Nonlinearities of organic electro-optic materials in nanoscale slots and implications for the optimum modulator design

Journal Article

Author(s):
Heni, Wolfgang; Haffner, Christian; Elder, Delwin L.; Tillack, Andreas F.; Fedoryshyn, Yuriy; Cottier, Raphael; Salamin, Yannick; Hössbacher, Claudia; Koch, Ueli iD; Cheng, Bojun; Robinson, Bruce; Dalton, Larry R.; Leuthold, Juerg iD

Nonlinearities of organic electro-optic materials in nanoscale slots and implications for the optimum modulator design

WOLFGANG HENI,[1,*] CHRISTIAN HAFFNER,[1] DELWIN L. ELDER,[2] ANDREAS F. TILLACK,[2] YURIY FEDORYSHYN,[1] RAPHAEL COTTIER,[1] YANNICK SALAMIN,[1] CLAUDIA HOESSBACHER,[1] UELI KOCH,[1] BOJUN CHENG,[1] BRUCE ROBINSON,[2] LARRY R. DALTON,[2] AND JUERG LEUTHOLD[1]

[1]*Institute of Electromagnetic Fields (IEF), ETH Zurich, 8092 Zurich, Switzerland*
[2]*Department of Chemistry, University of Washington, Seattle, WA 98195-1700, USA*
[*]*wheni@ethz.ch*

Abstract: The performance of highly nonlinear organic electro-optic (EO) materials incorporated into nanoscale slots is examined. It is shown that EO coefficients as large as 190 pm/V can be obtained in 150 nm wide plasmonic slot waveguides but that the coefficients decrease for narrower slots. Possible mechanism that lead to such a decrease are discussed. Monte-Carlo computer simulations are performed, confirming that chromophore-surface interactions are one important factor influencing the EO coefficient in narrow plasmonic slots. These highly nonlinear materials are of particular interest for applications in optical modulators. However, in modulators the key parameters are the voltage-length product $U_\pi L$ and the insertion loss rather than the linear EO coefficients. We show record-low voltage-length products of 70 Vµm and 50 Vµm for slot widths in the order of 50 nm for the materials JRD1 and DLD164, respectively. This is because the nonlinear interaction is enhanced in narrow slot and thereby compensates for the reduced EO coefficient. Likewise, it is found that lowest insertion losses are observed for slot widths in the range 60 to 100 nm.

References and links

1. R. W. Boyd, *Nonlinear Optics* (Academic, 2003).
2. Q. Wu and X. C. Zhang, "Ultrafast electro-optic field sensors," Appl. Phys. Lett. **68**(12), 1604–1606 (1996).
3. F. T. Sheehy, W. B. Bridges, and J. H. Schaffner, "60 GHz and 94 GHz antenna-coupled $LiNbO_3$ electrooptic modulators," IEEE Photonics Technol. Lett. **5**(3), 307–310 (1993).
4. W. B. Bridges, F. T. Sheehy, and J. H. Schaffner, "Wave-coupled $LiNbO_3$ electrooptic modulator for microwave and millimeter-wave modulation," IEEE Photonics Technol. Lett. **3**(2), 133–135 (1991).
5. Y. N. Wijayanto, H. Murata, and Y. Okamura, "Electrooptic millimeter-wave-lightwave signal converters suspended to gap-embedded patch antennas on low-*k* dielectric materials," IEEE J. Sel. Top. Quantum Electron. **19**(6), 33–41 (2013).
6. X. Zhang, A. Hosseini, H. Subbaraman, S. Wang, Q. Zhan, J. Luo, A. K.-Y. Jen, and R. T. Chen, "Integrated photonic electromagnetic field sensor based on broadband bowtie antenna coupled silicon organic hybrid modulator," J. Lightwave Technol. **32**(20), 3774–3784 (2014).
7. Y. Salamin, W. Heni, C. Haffner, Y. Fedoryshyn, C. Hoessbacher, R. Bonjour, M. Zahner, D. Hillerkuss, P. Leuchtmann, D. L. Elder, L. R. Dalton, C. Hafner, and J. Leuthold, "Direct conversion of free space millimeter waves to optical domain by plasmonic modulator antenna," Nano Lett. **15**(12), 8342–8346 (2015).
8. I.-C. Benea-Chelmus, C. Bonzon, C. Maissen, G. Scalari, M. Beck, and J. Faist, "Subcycle measurement of intensity correlations in the terahertz frequency range," Phys. Rev. A **93**(4), 043812 (2016).
9. C. V. McLaughlin, L. M. Hayden, B. Polishak, S. Huang, J. Luo, T.-D. Kim, and A. K. Jen, "Wideband 15THz response using organic electro-optic polymer emitter-sensor pairs at telecommunication wavelengths," Appl. Phys. Lett. **92**(15), 151107 (2008).
10. X. Zhang, C.-j. Chung, H. Subbaraman, Z. Pan, C.-T. Chen, and R. T. Chen, "Design of a plasmonic-organic hybrid slot waveguide integrated with a bowtie-antenna for terahertz wave detection," Proc. SPIE **975**, 975614 (2016).

11. K. D. Singer, M. G. Kuzyk, W. R. Holland, J. E. Sohn, S. J. Lalama, R. B. Comizzoli, H. E. Katz, and M. L. Schilling, "Electro-optic phase modulation and optical second-harmonic generation in corona-poled polymer films," Appl. Phys. Lett. **53**(19), 1800–1802 (1988).

12. L. Alloatti, D. Korn, C. Weimann, C. Koos, W. Freude, and J. Leuthold, "Second-order nonlinear silicon-organic hybrid waveguides," Opt. Express **20**(18), 20506–20515 (2012).

13. J. Zhang, E. Cassan, D. Gao, and X. Zhang, "Highly efficient phase-matched second harmonic generation using an asymmetric plasmonic slot waveguide configuration in hybrid polymer-silicon photonics," Opt. Express **21**(12), 14876–14887 (2013).

14. A. Nesic, R. Palmer, S. Koeber, D. Korn, S. Koenig, D. L. Elder, L. R. Dalton, W. Freude, and C. G. Koos, "Demonstration of difference frequency generation in a silicon slot waveguide," in *CLEO: 2014* (Optical Society of America, 2014), paper STh1I.2.

15. R. Sinha, M. Karabiyik, C. Al-Amin, P. K. Vabbina, D. Ö. Güney, and N. Pala, "Tunable room temperature THz sources based on nonlinear mixing in a hybrid optical and THz micro-ring resonator," Sci. Rep. **5**, 9422 (2015).

16. S. J. B. Yoo, C. Caneau, R. Bhat, M. A. Koza, A. Rajhel, and N. Antoniades, "Wavelength conversion by difference frequency generation in algaas waveguides with periodic domain inversion achieved by wafer bonding," Appl. Phys. Lett. **68**(19), 2609–2611 (1996).

17. M. Lauermann, C. Weimann, A. Knopf, W. Heni, R. Palmer, S. Koeber, D. L. Elder, W. Bogaerts, J. Leuthold, L. R. Dalton, C. Rembe, W. Freude, and C. Koos, "Integrated optical frequency shifter in silicon-organic hybrid (SOH) technology," Opt. Express **24**(11), 11694–11707 (2016).

18. D. Chen, H. R. Fetterman, A. Chen, W. H. Steier, L. R. Dalton, W. Wang, and Y. Shi, "Demonstration of 110 GHz electro-optic polymer modulators," Appl. Phys. Lett. **70**(25), 3335–3337 (1997).

19. Y. Shi, C. Zhang, H. Zhang, J. H. Bechtel, L. R. Dalton, B. H. Robinson, and W. H. Steier, "Low (Sub-1-volt) halfwave voltage polymeric electro-optic modulators achieved by controlling chromophore shape," Science **288**(5463), 119–122 (2000).

20. M. Lee, H. E. Katz, C. Erben, D. M. Gill, P. Gopalan, J. D. Heber, and D. J. McGee, "Broadband modulation of light by using an electro-optic polymer," Science **298**(5597), 1401–1403 (2002).

21. T. Baehr-Jones, M. Hochberg, G. Wang, R. Lawson, Y. Liao, P. Sullivan, L. Dalton, A. Jen, and A. Scherer, "Optical modulation and detection in slotted Silicon waveguides," Opt. Express **13**(14), 5216–5226 (2005).

22. J. Leuthold, C. Koos, W. Freude, L. Alloatti, R. Palmer, D. Korn, J. Pfeifle, M. Lauermann, R. Dinu, S. Wehrli, M. Jazbinsek, P. Gunter, M. Waldow, T. Wahlbrink, J. Bolten, H. Kurz, M. Fournier, J.-M. Fedeli, H. Yu, and W. Bogaerts, "Silicon-organic hybrid electro-optical devices," IEEE J. Sel. Top. Quantum Electron. **19**(6), 114–126 (2013).

23. Y. Jouane, Y. C. Chang, D. Zhang, J. Luo, A. K. Jen, and Y. Enami, "Unprecedented highest electro-optic coefficient of 226 pm/V for electro-optic polymer/TiO_2 multilayer slot waveguide modulators," Opt. Express **22**(22), 27725–27732 (2014).

24. D. L. K. Eng, S. Kozacik, S. Shi, B. C. Olbricht, and D. W. Prather, "All-polymer modulator for high frequency low drive voltage applications," Proc. SPIE **8983**, 898316 (2014).

25. C. Koos, J. Leuthold, W. Freude, M. Kohl, L. Dalton, W. Bogaerts, A. L. Giesecke, M. Lauermann, A. Melikyan, S. Koeber, S. Wolf, C. Weimann, S. Muehlbrandt, K. Koehnle, J. Pfeifle, W. Hartmann, Y. Kutuvantavida, S. Ummethala, R. Palmer, D. Korn, L. Alloatti, P. C. Schindler, D. L. Elder, T. Wahlbrink, and J. Bolten, "Silicon-organic hybrid (SOH) and plasmonic-organic hybrid (POH) integration," J. Lightwave Technol. **34**(2), 256–268 (2016).

26. S. Abel, T. Stöferle, C. Marchiori, D. Caimi, L. Czornomaz, M. Stuckelberger, M. Sousa, B. J. Offrein, and J. Fompeyrine, "A hybrid barium titanate–silicon photonics platform for ultraefficient electro-optic tuning," J. Lightwave Technol. **34**(8), 1688–1693 (2016).

27. R. S. Weis and T. K. Gaylord, "Lithium niobate: Summary of physical properties and crystal structure," Appl. Phys., A Mater. Sci. Process. **37**(4), 191–203 (1985).

28. W. W. Jin, P. V. Johnston, D. L. Elder, A. F. Tillack, B. C. Olbricht, J. S. Song, P. J. Reid, R. M. Xu, B. H. Robinson, and L. R. Dalton, "Benzocyclobutene barrier layer for suppressing conductance in nonlinear optical devices during electric field poling," Appl. Phys. Lett. **104**(24), 884829 (2014).

29. X. Zhang, A. Hosseini, H. Subbaraman, J. Luo, A. K. Y. Jen, C.-j. Chung, H. Yan, Z. Pan, R. L. Nelson, and R. T. Chen, "Broadband energy-efficient optical modulation by hybrid integration of silicon nanophotonics and organic electro-optic polymer," arXiv 1503.01912 (2014).

30. T. Gray, T.-D. Kim, D. B. Knorr, Jr., J. Luo, A. K. Y. Jen, and R. M. Overney, "Mesoscale dynamics and cooperativity of networking dendronized nonlinear optical molecular glasses," Nano Lett. **8**(2), 754–759 (2008).

31. T.-D. Kim, J. Luo, Y.-J. Cheng, Z. Shi, S. Hau, S.-H. Jang, X.-H. Zhou, Y. Tian, B. Polishak, S. Huang, H. Ma, L. R. Dalton, and A. K. Y. Jen, "Binary chromophore systems in nonlinear optical dendrimers and polymers for large electrooptic activities†," J. Phys. Chem. C **112**(21), 8091–8098 (2008).

32. X.-H. Zhou, J. Luo, S. Huang, T.-D. Kim, Z. Shi, Y.-J. Cheng, S.-H. Jang, D. B. Knorr, Jr., R. M. Overney, and A. K. Y. Jen, "Supramolecular self-assembled dendritic nonlinear optical chromophores: Fine-tuning of arene–perfluoroarene interactions for ultralarge electro-optic activity and enhanced thermal stability," Adv. Mater. **21**(19), 1976–1981 (2009).

33. M. Li, S. Huang, X.-H. Zhou, Y. Zang, J. Wu, Z. Cui, J. Luo, and A. K. Y. Jen, "Poling efficiency enhancement of tethered binary nonlinear optical chromophores for achieving an ultrahigh $n^3 r_{33}$ figure-of-merit of 2601 pm V^{-1}," J. Mater. Chem. C Mater. Opt. Electron. Devices **3**(26), 6737–6744 (2015).

34. R. Palmer, S. Koeber, D. L. Elder, M. Woessner, W. Heni, D. Korn, M. Lauermann, W. Bogaerts, L. Dalton, W. Freude, J. Leuthold, and C. Koos, "High-speed, low drive-voltage silicon-organic hybrid modulator based on a binary-chromophore electro-optic material," J. Lightwave Technol. **32**(16), 2726–2734 (2014).

35. A. Melikyan, L. Alloatti, A. Muslija, D. Hillerkuss, P. C. Schindler, J. Li, R. Palmer, D. Korn, S. Muehlbrandt, D. Van Thourhout, B. Chen, R. Dinu, M. Sommer, C. Koos, M. Kohl, W. Freude, and J. Leuthold, "High-speed plasmonic phase modulators," Nat. Photonics **8**(3), 229–233 (2014).

36. W. Heni, C. Haffner, B. Baeuerle, Y. Fedoryshyn, A. Josten, D. Hillerkuss, J. Niegemann, A. Melikyan, M. Kohl, D. L. Elder, L. R. Dalton, C. Hafner, and J. Leuthold, "108 Gbit/s plasmonic Mach-Zehnder modulator with > 70-GHz electrical bandwidth," J. Lightwave Technol. **34**(2), 393–400 (2016).

37. C. Hoessbacher, A. Josten, B. Baeuerle, Y. Fedoryshyn, H. Hettrich, Y. Salamin, W. Heni, C. Haffner, C. Kaiser, R. Schmid, D. L. Elder, D. Hillerkuss, M. Möller, L. R. Dalton, and J. Leuthold, "Plasmonic modulator with >170 GHz bandwidth demonstrated at 100 GBd NRZ," Opt. Express **25**(3), 1762–1768 (2017).

38. C. Haffner, W. Heni, Y. Fedoryshyn, A. Josten, B. Baeuerle, C. Hoessbacher, Y. Salamin, U. Koch, N. Đorđević, P. Mousel, R. Bonjour, A. Emboras, D. Hillerkuss, P. Leuchtmann, D. L. Elder, L. R. Dalton, C. Hafner, and J. Leuthold, "Plasmonic organic hybrid modulators—scaling highest speed photonics to the microscale," Proc. IEEE **104**(12), 2362–2379 (2016).

39. W. Heni, C. Haffner, P. V. Johnston, D. L. Elder, Y. Fedoryshyn, R. Cottier, Y. Salamin, C. Hoessbacher, A. F. Tillack, L. R. Dalton, C. Hafner, and J. Leuthold, "Optimizing plasmonic modulators for in-device nonlinearities of up to 275 pm/v," in *Integrated Photonics Research, Silicon and Nanophotonics*(Optical Society of America, 2016), paper ITu1A.1.

40. C. Haffner, W. Heni, Y. Fedoryshyn, J. Niegemann, A. Melikyan, D. L. Elder, B. Baeuerle, Y. Salamin, A. Josten, U. Koch, C. Hoessbacher, F. Ducry, L. Juchli, A. Emboras, D. Hillerkuss, M. Kohl, L. R. Dalton, C. Hafner, and J. Leuthold, "All-plasmonic Mach–Zehnder modulator enabling optical high-speed communication at the microscale," Nat. Photonics **9**(8), 525–528 (2015).

41. W. Heni, C. Hoessbacher, C. Haffner, Y. Fedoryshyn, B. Baeuerle, A. Josten, D. Hillerkuss, Y. Salamin, R. Bonjour, A. Melikyan, M. Kohl, D. L. Elder, L. R. Dalton, C. Hafner, and J. Leuthold, "High speed plasmonic modulator array enabling dense optical interconnect solutions," Opt. Express **23**(23), 29746–29757 (2015).

42. C. Hoessbacher, Y. Salamin, Y. Fedoryshyn, W. Heni, A. Josten, B. Baeuerle, C. Haffner, M. Zahner, H. Chen, D. L. Elder, S. Wehrli, D. Hillerkuss, D. Van Thourhout, J. Van Campenhout, L. R. Dalton, C. Hafner, and J. Leuthold, "Optical interconnect with densely integrated plasmonic modulator and germanium photodetector arrays," in *Optical Fiber Communication Conference* (Optical Society of America, 2016), paper Th1F.6.

43. S. Koeber, R. Palmer, M. Lauermann, W. Heni, D. L. Elder, D. Korn, M. Woessner, L. Alloatti, S. Koenig, P. C. Schindler, H. Yu, W. Bogaerts, L. R. Dalton, W. Freude, J. Leuthold, and C. Koos, "Femtojoule electro-optic modulation using a silicon-organic hybrid device," Light Sci. Appl. **4**(2), e255 (2015).

44. Y. V. Pereverzev, K. N. Gunnerson, O. V. Prezhdo, P. A. Sullivan, Y. Liao, B. C. Olbricht, A. J. P. Akelaitis, A. K. Y. Jen, and L. R. Dalton, "Guest–host cooperativity in organic materials greatly enhances the nonlinear optical response," J. Phys. Chem. C **112**(11), 4355–4363 (2008).

45. X. Wang, C.-Y. Lin, S. Chakravarty, J. Luo, A. K.-Y. Jen, and R. T. Chen, "Effective in-device r33 of 735 pm/V on electro-optic polymer infiltrated silicon photonic crystal slot waveguides," Opt. Lett. **36**(6), 882–884 (2011).

46. "Gigoptix inc.," *http://www.gigoptix.com*.

47. V. Katopodis, P. Groumas, Z. Zhang, R. Dinu, E. Miller, A. Konczykowska, J. Y. Dupuy, A. Beretta, A. Dede, J. H. Choi, P. Harati, F. Jorge, V. Nodjiadjim, M. Riet, G. Cangini, A. Vannucci, N. Keil, H. G. Bach, N. Grote, H. Avramopoulos, and C. Kouloumentas, "Polymer enabled 100 Gbaud connectivity for datacom applications," Opt. Commun. **362**, 13–21 (2016).

48. D. Jin, H. Chen, A. Barklund, J. Mallari, G. Yu, E. Miller, and R. Dinu, "Eo polymer modulators reliability study," Proc. SPIE **7599**, 75990H (2010).

49. R. Palmer, L. Alloatti, D. Korn, P. C. Schindler, M. Baier, J. Bolten, T. Wahlbrink, M. Waldow, R. Dinu, W. Freude, C. Koos, and J. Leuthold, "Low power mach-zehnder modulator in silicon-organic hybrid technology," IEEE Photonics Technol. Lett. **25**(13), 1226–1229 (2013).

50. R. Palmer, L. Alloatti, D. Korn, P. C. Schindler, R. Schmogrow, W. Heni, S. Koenig, J. Bolten, T. Wahlbrink, M. Waldow, H. Yu, W. Bogaerts, P. Verheyen, G. Lepage, M. Pantouvaki, J. Van Campenhout, P. Absil, R. Dinu, W. Freude, C. Koos, and J. Leuthold, "Silicon-organic hybrid MZI modulator generating OOK, BPSK and 8-ASK signals for up to 84 Gbit/s," IEEE Photonics J. **5**(2), 6600907 (2013).

51. X. Zhang, C.-J. Chung, A. Hosseini, H. Subbaraman, J. Luo, A. K. Y. Jen, R. L. Nelson, C. Y. C. Lee, and R. T. Chen, "High performance optical modulator based on electro-optic polymer filled silicon slot photonic crystal waveguide," J. Lightwave Technol. **34**(12), 2941–2951 (2016).

52. "Soluxra, llc," *http://www.soluxra.com/*.

53. A. Melikyan, K. Koehnle, M. Lauermann, R. Palmer, S. Koeber, S. Muehlbrandt, P. C. Schindler, D. L. Elder, S. Wolf, W. Heni, C. Haffner, Y. Fedoryshyn, D. Hillerkuss, M. Sommer, L. R. Dalton, D. Van Thourhout, W. Freude, M. Kohl, J. Leuthold, and C. Koos, "Plasmonic-organic hybrid (POH) modulators for OOK and BPSK signaling at 40 Gbit/s," Opt. Express **23**(8), 9938–9946 (2015).

54. Y. Enami, H. Nakamura, J. Luo, and A. K. Y. Jen, "Analysis of efficiently poled electro-optic polymer/TiO$_2$ vertical slot waveguide modulators," Opt. Commun. **362**, 77–80 (2016).

55. R. Himmelhuber, O. D. Herrera, R. Voorakaranam, L. Li, A. M. Jones, R. A. Norwood, J. Luo, A. K. Y. Jen, and N. Peyghambarian, "A silicon-polymer hybrid modulator;design, simulation and proof of principle," J. Lightwave Technol. **31**(24), 4067–4072 (2013).

56. L. Dalton, P. Günter, M. Jazbinsek, O. Kwon, and P. Sullivan, *Organic Electro-optics and Photonics* (Cambridge, 2015).

57. W. Jin, P. V. Johnston, D. L. Elder, K. T. Manner, K. E. Garrett, W. Kaminsky, R. Xu, B. H. Robinson, and L. R. Dalton, "Structure–function relationship exploration for enhanced thermal stability and electro-optic activity in monolithic organic nlo chromophores," J. Mater. Chem. C Mater. Opt. Electron. Devices **4**(15), 3119–3124 (2016).

58. D. L. Elder, S. J. Benight, J. Song, B. H. Robinson, and L. R. Dalton, "Matrix-assisted poling of monolithic bridge-disubstituted organic nlo chromophores," Chem. Mater. **26**(2), 872–874 (2014).

59. Y. Enami, Y. Jouane, J. Luo, and A. K. Y. Jen, "Enhanced conductivity of sol-gel silica cladding for efficient poling in electro-optic polymer/TiO$_2$ vertical slot waveguide modulators," Opt. Express **22**(24), 30191–30199 (2014).

60. X. Zhang, A. Hosseini, S. Chakravarty, J. Luo, A. K. Y. Jen, and R. T. Chen, "Wide optical spectrum range, subvolt, compact modulator based on an electro-optic polymer refilled silicon slot photonic crystal waveguide," Opt. Lett. **38**(22), 4931–4934 (2013).

61. X. Zhang, A. Hosseini, X. Lin, H. Subbaraman, and R. T. Chen, "Polymer-based hybrid-integrated photonic devices for silicon on-chip modulation and board-level optical interconnects," IEEE J. Sel. Top. Quantum Electron. **19**(6), 196–210 (2013).

62. L. R. Dalton, P. A. Sullivan, and D. H. Bale, "Electric field poled organic electro-optic materials: state of the art and future prospects," Chem. Rev. **110**(1), 25–55 (2010).

63. J. J. Wolff and R. Wortmann, "Organic materials for second-order non-linear optics," Adv. Phys. Org. Chem. **32**, 121–217 (1999).

64. D. M. Burland, R. D. Miller, and C. A. Walsh, "Second-order nonlinearity in poled-polymer systems," Chem. Rev. **94**(1), 31–75 (1994).

65. L. R. Dalton, S. J. Benight, L. E. Johnson, D. B. Knorr, Jr., I. Kosilkin, B. E. Eichinger, B. H. Robinson, A. K. Y. Jen, and R. M. Overney, "Systematic nanoengineering of soft matter organic electro-optic materials," Chem. Mater. **23**(3), 430–445 (2011).

66. B. Robinson and L. Dalton, "Monte Carlo statistical mechanical simulations of the competition of intermolecular electrostatic and poling-field interactions in defining macroscopic electro-optic activity for organic chromophore/polymer materials," J. Phys. Chem. A **104**(20), 4785–4795 (2000).

67. S. J. Benight, L. E. Johnson, R. Barnes, B. C. Olbricht, D. H. Bale, P. J. Reid, B. E. Eichinger, L. R. Dalton, P. A. Sullivan, and B. H. Robinson, "Reduced dimensionality in organic electro-optic materials: theory and defined order," J. Phys. Chem. B **114**(37), 11949–11956 (2010).

68. J. Oudar and D. Chemla, "Hyperpolarizabilities of the nitroanilines and their relations to the excited state dipole moment," J. Chem. Phys. **66**(6), 2664–2668 (1977).

69. Y.-J. Wang and G. Carlisle, "Optical properties of disperse-red-1-doped nematic liquid crystal," J. Mater. Sci. Mater. Electron. **13**(3), 173–178 (2002).

70. T. Pliška, W.-R. Cho, J. Meier, A.-C. Le Duff, V. Ricci, A. Otomo, M. Canva, G. I. Stegeman, P. Raimond, and F. Kajzar, "Comparative study of nonlinear-optical polymers for guided-wave second-harmonic generation at telecommunication wavelengths," J. Opt. Soc. Am. B **17**(9), 1554–1564 (2000).

71. P. V. Johnston, "Structure function paradigms of organic electrooptic materials," in *PhD Thesis* (University of Washington, 2016).

72. A. F. Tillack, "Electro-optic material design criteria derived from condensed matter simulations using the level-of-detail coarse-graining approach," in *PhD Thesis* (University of Washington, 2015).

73. D. B. Knorr, Jr., S. J. Benight, B. Krajina, C. Zhang, L. R. Dalton, and R. M. Overney, "Nanoscale phase analysis of molecular cooperativity and thermal transitions in dendritic nonlinear optical glasses," J. Phys. Chem. B **116**(46), 13793–13805 (2012).

74. S. J. Benight, D. B. Knorr, Jr., L. E. Johnson, P. A. Sullivan, D. Lao, J. Sun, L. S. Kocherlakota, A. Elangovan, B. H. Robinson, R. M. Overney, and L. R. Dalton, "Nano-engineering lattice dimensionality for a soft matter organic functional material," Adv. Mater. **24**(24), 3263–3268 (2012).

75. D. R. Kanis, M. A. Ratner, and T. J. Marks, "Design and construction of molecular assemblies with large second-order optical nonlinearities. Quantum chemical aspects," Chem. Rev. **94**(1), 195–242 (1994).

76. A. F. Tillack, L. E. Johnson, B. E. Eichinger, and B. H. Robinson, "Systematic generation of anisotropic coarse-grained lennard-jones potentials and their application to ordered soft matter," J. Chem. Theory Comput. **12**(9), 4362–4374 (2016).

77. A. F. Tillack and B. H. Robinson, "Toward optimal eo response from onlo chromophores: A statistical mechanics study of optimizing shape," J. Opt. Soc. Am. B **33**(12), E121–E129 (2016).

78. L. Dalton, W. Steier, B. Robinson, C. Zhang, A. Ren, S. Garner, A. Chen, T. Londergan, L. Irwin, B. Carlson, L. Fifield, G. Phelan, C. Kincaid, J. Amend, and A. Jen, "From molecules to opto-chips: Organic electro-optic materials," J. Mater. Chem. **9**(9), 1905–1920 (1999).

79. P. P. Klein, "On the ellipsoid and plane intersection equation," Appl. Math. **3**(11), 1634–1640 (2012).

80. H. Heinz, R. Vaia, B. Farmer, and R. Naik, "Accurate simulation of surfaces and interfaces of face-centered cubic metals using 12− 6 and 9− 6 Lennard-Jones potentials," J. Phys. Chem. C **112**(44), 17281–17290 (2008).

81. J.-M. Brosi, C. Koos, L. C. Andreani, M. Waldow, J. Leuthold, and W. Freude, "High-speed low-voltage electro-optic modulator with a polymer-infiltrated silicon photonic crystal waveguide," Opt. Express **16**(6), 4177–4191 (2008).
82. L. Alloatti, D. Korn, R. Palmer, D. Hillerkuss, J. Li, A. Barklund, R. Dinu, J. Wieland, M. Fournier, J. Fedeli, H. Yu, W. Bogaerts, P. Dumon, R. Baets, C. Koos, W. Freude, and J. Leuthold, "42.7 Gbit/s electro-optic modulator in silicon technology," Opt. Express **19**(12), 11841–11851 (2011).

1. Introduction

Large electro-optic (EO) coefficients [1] are beneficial for efficient operation of e.g. field-sensors [2–10], for nonlinear frequency conversion [11–17] or electro-optical data modulation [18–26]. EO modulators are of particular importance as they are ubiquitously used in optical communications. The efficiency of EO modulators depends on the strength of the EO coefficient. In practice however, the device performance not only depends on the EO coefficient but also on the dimensions of the waveguide and confinement of the light to the EO material. In this context the voltage-length product has emerged as a useful figure of merit. It gives the active device length and voltage required to switch from the on- to the off-state. The ultimate goal of a modulator design is the fabrication of devices with the smallest possible voltage-length product (i.e. smallest footprint with the least required voltage) and the lowest losses.

To this day optical modulators for communications rely almost exclusively on $LiNbO_3$ with an EO coefficient of $r_{33} \approx 34$ pm/V [27], offering voltage-length products of $U_\pi L \approx 1\text{-}10$ Vcm. Larger EO coefficients can be provided by organic EO materials with reported bulk EO coefficients of $r_{33} \gtrsim 400$ pm/V [28–33]. However, when these organic materials are deposited onto a chip for integrated optical applications, the reported EO coefficients are often below the values reported for bulk materials [29–32]. For example, when the organic EO materials are applied to slot waveguide configurations featuring slot widths below 400 nm it becomes more challenging to achieve large in-device EO coefficients. Only recently EO coefficients of up to $r_{33} = 230$ pm/V (at 1550 nm) were measured in 150 nm wide silicon slot waveguides [34] while the same material provided EO coefficients of up to $r_{33} = 273$ pm/V (at 1310 nm) in bulk materials.

In this communication, in a first step we investigate the EO activity of the organic EO materials JRD1 and DLD164. In-device EO coefficients of 190 pm/V have been found in plasmonic slot-waveguides with widths in the order of 150 nm and wider. The EO coefficients significantly decrease for narrower slots though, see Fig. 1. Possible reasons for the decrease of the EO coefficient are discussed. In a second step, we investigate the performance of these materials in a new generation of plasmonic modulators [35,36] with respect to the width of the plasmonic slot waveguide. It is shown, that the plasmonic sub-diffraction light confinement not only compensates for the decrease of the EO coefficient in narrow slot waveguides, but also allows for shorter devices and therefore results in lower insertion losses for narrower slot waveguides. So, for instance, record-low voltage-length products of 50 to 70 Vµm are found for slot widths in the order of 60 nm. The lowest insertion loss is observed for slot widths in the range of 60 to 100 nm. The ideal nonlinear device should thus feature slot widths in the order of 60 nm. Implementing a 60 nm slot-width in an EO modulator we can demonstrate on- to off-operation with voltages as low as $U_\pi = 1.4$ V. This demonstrates that the plasmonic modulator technology not only offers high-speed >170 GHz operation [37] and most-compact footprints [38], but can also offer low operation voltages in the order of 1 V compatible with CMOS transistors voltage levels.
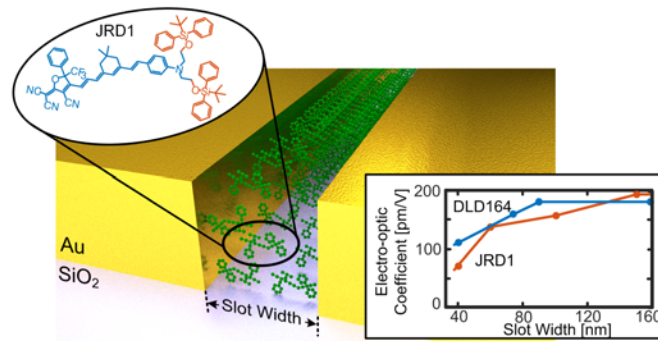
Fig. 1. Artistic view of a plasmonic slot waveguide filled with an organic EO material (JRD1, inset). A dependence of the EO coefficient on the slot waveguide width is experimentally investigated for the materials JRD1 and DLD164. EO coefficients of 190 pm/V are found for wide slots while these values decrease for narrower slots.

The article is organized in two main chapters. Chapter 2 focuses on the organic EO materials and their electro-optic coefficient and Chapter 3 discusses the application of such organic EO materials in plasmonic-organic hybrid modulators. Chapter 2 starts with Section 2.1 discussing the performance of state-of-the-art organic EO materials when incorporated into nanoscale slot waveguides. Section 2.2 describes the materials used in this work and connects the molecular nonlinearity of the chromophores and the macroscopic EO coefficients of their materials. Possible origins of the slot width dependent EO coefficient are discussed in Section 2.3. Chapter 3 starts with Section 3.1 to introduce the plasmonic-organic hybrid (POH) Mach-Zehnder modulator (MZM) that will be subsequently used for the EO characterization of JRD1, including device poling and the slot-width dependent EO coefficient. Section 3.2 describes the influence of the slot-width dependent in-device nonlinearity on the modulator performance and discusses the optimum modulator design parameters.

2. The electro-optic coefficient and its dependence on the geometry

2.1. State-of-the-art organic electro-optic materials in nanophotonic devices

The performance of EO materials in nanophotonic devices depends strongly on the dimensions of the active region. In bulk materials, with material films having thicknesses from hundreds of nm to several µm, large EO coefficients of $r_{33} > 400$ pm/V [29–33] can be achieved. However, when organic EO materials are applied to horizontal silicon or metal slot waveguide structures the large bulk values typically cannot be reached. This section discusses the slot-width dependence of in-device EO coefficients of state-of-the-art organic EO materials.

In this work we investigate the slot-width dependence of the organic EO materials JRD1 [39] and DLD164 [7, 36, 38, 40–42]. We observe a distinct decrease in the EO coefficient with decreasing slot width. Figure 2 depicts the slot width dependent EO coefficients for the two investigated materials and additional state-of-the-art organic EO materials. For DLD164 an additional measurement performed in a silicon-organic hybrid (SOH) modulator [43] with a 160 nm wide slot is included. Table 1 summarizes the corresponding data of Fig. 2. Note that the calculation of the EO coefficient in [39] was performed with a refractive index of 1.62 at 1600 nm. New measurements indicated a refractive index of 1.8 at 1600 nm. While the measured device performance is not influenced, calculated values such as the EO coefficient have been adapted. Compared to [39], the second-order nonlinearity slightly increases to $\chi^{(2)}_{333} = 1020$ pm/V, therefore the maximum EO coefficient r_{33} calculates to 193

pm/V. All calculated values in this article are derived using the measured refractive index given in this manuscript.

Comparing the EO coefficient of the investigated materials JRD1 and DLD164 to reported values of the independent studies (Refs [34, 43–55].) indicates a similar slot-width dependent EO coefficient in other materials and material composites. These reported in-device nonlinearities were characterized in silicon slot waveguide based modulators [22]. The largest in-device nonlinearity reported so far was achieved with the binary chromophore organic glass (BCOG) YLD124/PSLD41 [34, 44]. Yet, most commonly used materials are based on guest-host polymer systems. These include AJCKL1/APC [45] and commercially-available materials such as GigOptix M3 [46–50], Soluxra SEO100 [52, 54, 55], and Soluxra SEO125 [51–53].
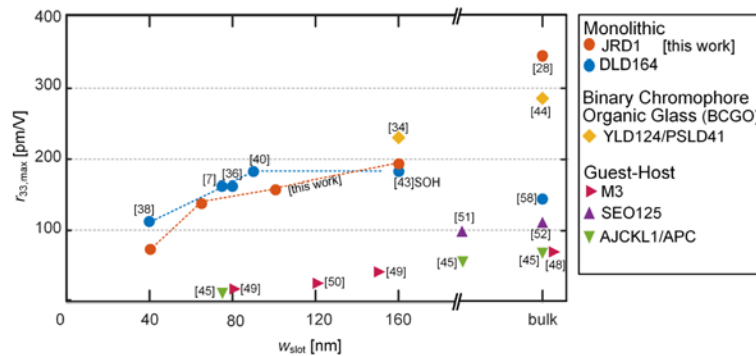

Fig. 2. Maximum reported EO coefficients as a function of the slot width. For all reviewed materials a strong slot-width dependence of the EO coefficient is found. Monolithic material systems show a more than 10 times higher EO coefficient than guest-host systems for slot widths below 80 nm, indicating that these material systems may potentially be better suitable for nanoscale photonic applications. (Device EO coefficients measured around 1550 nm, bulk values measured at 1310 nm.)

All reviewed materials show a strong slot-width dependence of the EO coefficient. Possible origins for this dependence are discussed in Section 2.3. For the few reported slot widths below 100 nm the performance of guest-host based materials is reduced to EO coefficients below 50 pm/V. At similar slot widths, monolithic material systems feature approximately 4-times larger EO coefficients in the range of 150-200 pm/V. Even at further reduced slot widths below 80 nm, these monolithic materials offer much larger EO coefficients than guest-host based materials. This indicates that these monolithic material systems may be better suited for nanoscale photonic applications. Note that the bulk values plotted here have been taken from measurements performed at a wavelength of 1310 nm while all in device-measurements have been performed around 1550 nm. The EO coefficient typically is higher at shorter wavelengths, so that the bulk values if measured at 1550 nm would in fact be lower.

In addition to the EO coefficient, the refractive index n and the glass transition temperature T_g are important material properties to be taken into account for the in-device application of these materials (see Table 1). A low T_g material allows for easy material poling (see Section 2.2) at low temperatures. However, a low T_g also asks for moderate operation temperatures. The commercial materials GigOptix M3 and Soluxra SEO100, and SEO125 have demonstrated long-term stability at 85°C satisfying Telcorida standards An alternative to these materials with an inherently high T_g are materials, which can be crosslinked to elevate the material glass transition subsequent to electric field poling [56].

Table 1. State-of-the-art organic electro-optic materials.

	$r_{33,\text{bulk}}$ [pm /V] 1310 nm	$r_{33,\text{in-device}}$ ($w_{\text{slot}} \approx 60$-80 nm) [pm /V] 1550 nm	$r_{33,\text{in-device}}$ ($w_{\text{slot}} \approx 100$-120 nm) [pm /V] 1550 nm	$r_{33,\text{in-device}}$ ($w_{\text{slot}} \geq 150$ nm) [pm /V] 1550 nm	n 1310 nm /1550 nm	$\chi^{(2)}_{333}$ in-device [pm/V] 1550 nm	T_g [°C]
JRD1 [57]	343 / 556[a] [28]	136[c] [this work]	156[c] [this work]	193[c] [this work]	1.87 / 1.81	1024[c]	82 [57]
DLD164 [58]	137 [58]	160 [36]	180 [40]	180 [43]	1.9 / 1.83	1010	66 [58]
YLD124/ PSLD41 [44]	285 [44]	-	-	230 [34]	1.77 / 1.73 [44]	1030	97 [34]
BNLO [33] [b]	273 [33]	-	-	-	2.21/- [33]		117 [33]
25%YLD124/ PMMA	118 [58]	-	-	30 [34]	1.6 / 1.58[d]	125[d]	105 [58]
Soluxra SEO100 [52]	110/260[a] [54]	-	-	132 [55]	/ 1.71 [59]	564	-
Soluxra SEO125 [52]	125 [60]	-	-	98 [51]	- / 1.63 [51]	346	150 [51]
GigOptix M3 [46]	86 [47,48]	15 [49]	23 [50]	40 [49]	- / 1.68	160	168 [46]
25%AJCKL1/ APC	90 [45] (1550 nm75 pm/V)	10	-	59 [45]	- / 1.63 [61]	208	145 [45]

[a] with charge blocking layer. [b] Binary nonlinear optical chromophore C1 in [33]. [c] measured at 1600 nm, larger r_{33} is expected at lower wavelengths. [d] [34] gives an refractive index of 1.7 at 1550 nm for 25%YLD124/PMMA. Ellipsometric measurements result in n(1550 nm) = 1.58. To calculate $\chi^{(2)}_{333}$ the refractive index and the EO coefficient given in [34] are used.

2.2. Organic Electro-Optic Materials – From Microscopic to Macroscopic Nonlinearities

This section describes microscopic properties of the monolithic organic EO materials JRD1 and DLD164 investigated in this work as well as how these microscopic properties are translated to their macroscopic nonlinear behavior.

In general, EO chromophores are randomly oriented upon solution deposition, Fig. 2(a). To achieve macroscopic second-order nonlinearity, those molecules have to be aligned non-centrosymmetrically [62, 63]. This can be achieved by electric-field poling [62, 64], where an electric field is applied to the material while the material is heated near its glass transition temperature. During this process, the molecules reorient due to the torque on their molecular dipole moments $\vec{\mu}$, in response to the electric field, see Fig. 2(b).
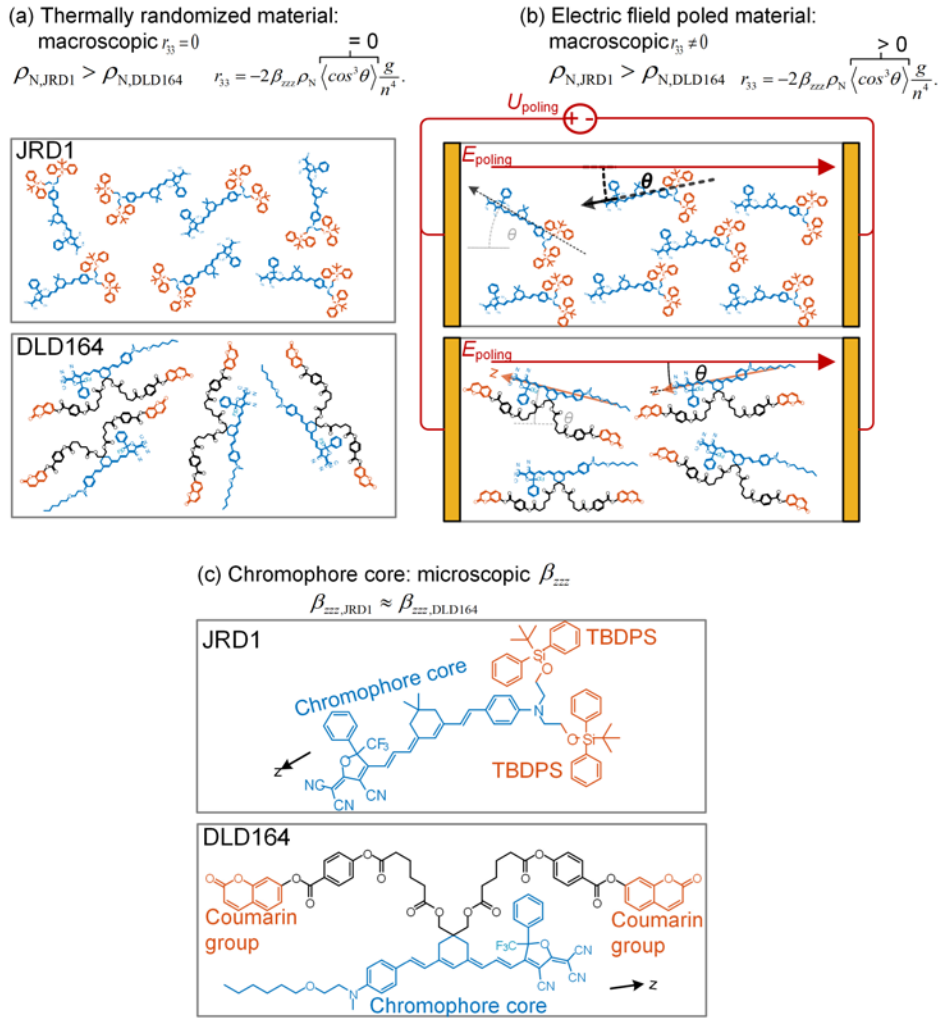
Fig. 3. (a) Thermally randomized order of the material after deposition. JRD1 offers a higher chromophore density ρ_N than DLD164. The randomized order results in an average order of $\cos^3 \theta = 0$. (b) Upon electric field poling the chromophores align along the poling field E_{poling}. The angle θ between the dipole axis $\vec{\mu}$ and the poling field describes the efficiency of the poling process. The ordering of all molecules in one direction results in $\langle cos^3 \rangle > 0$ and therefore $r_{33} > 0$. (c) Chemical structure of the chromophores. Both materials share the commonly used amine donor – π bridge – tricyanofuran acceptor motif chromophore core. JRD1 features two sterically bulky *tert*-butyldiphenylsilyl (TBDPS) functional groups, DLD164 features two coumarin-based pendent side chains.

The macroscopic second-order nonlinearity r_{33} achievable during electric field poling can be related to its microscopic material properties [65]:

$$r_{33} = -2\beta_{zzz}\rho_N \left\langle \cos^3 \theta \right\rangle \frac{g}{n^4}, \qquad (1)$$

where, the microscopic nonlinearity of the molecules along its dipole axis is described by its first-order hyperpolarizability β_{zzz}. The chromophore number density is given by ρ_N. The average degree of orientation of the chromophores is described by the average acentric order

parameter $\left\langle cos^3 \right\rangle > 0$, where θ describes the angle between the external electric poling field E_z and the dipole moment of the individual chromophores $\vec{\mu}$, Fig. 2(b). In a perfectly ordered system all molecules would be aligned parallel to the electric poling field E_p meaning $\theta = 0$ and $cos^3 \theta = 1$. However, due to thermal effects an upper limit to acentric order may be given by the Langevin limit as $cos^3 \theta \approx \vec{\mu}E / 5kT$ [66, 67]. To take into account partial field screening in the material the Lorentz-Onsager local field factor g [62] is included, n is the (wavelength dependent) index of refraction at the wavelength of interest.

To achieve largest EO coefficients r_{33}, each of the contributors to Eq. (1) should be maximized, but unfortunately, some of the contributions are not necessarily independent and may work counter to one another. β_{zzz} can be tuned using synthetic chemistry guided by theoretical modeling [62]. Increasing β_{zzz} generally involves having a strong electron donor and a strong electron acceptor separated by a rigid polyene π-bridge. β_{zzz} increases as distance between the donor and acceptor increases, which also redshifts the chromophore absorbance according to the two-state model [63, 68] and could contribute to optical loss if it is too close to the operation wavelength of the modulator. As β_{zzz} increases, the dipole moment $\vec{\mu}$ also increases, although the dependence on length is not as strong. Electrostatic attraction proportional to $\vec{\mu}^2$ drives dipolar molecules to assemble into antiparallel pairs (dipolar coupling) that are centrosymmetric. This coupling energy must be overcome by the poling field to get good alignment.

While dipole moments of chromophores used a decade or more ago, such as DR-1, had dipole moments in the 8-10 D range [69, 70], the best chromophores today have dipole moments in the 30 D range, which dramatically increases the magnitude of dipolar intermolecular interaction and reduces the maximum $cos^3 \theta$ achievable at a certain poling field. The strength of dipolar coupling is inversely proportional to the organic EO chromophore intermolecular distance, so centrosymmetric ordering can be reduced by diluting the chromophores in a host polymer, resulting in increased $cos^3 \theta$ upon poling. However, diluting organic EO chromophore in a host polymer reduces ρ_N. Therefore, $\rho_N \cos^3 \theta$, often called the loading parameter, can be thought of as a single constraint to optimize.

We investigate two organic EO materials in more detail, JRD1 [28, 57, 71] and DLD164 [58], both optimized for a high loading parameter $\rho_N \cos^3 \theta$. While sharing a similar chromophore core designed for large nonlinearity and low absorbance in the telecom wavelength range (1310 nm and 1550 nm), see below, JRD1 and DLD164 represent different approaches to optimizing the loading parameter $\rho_N \cos^3 \theta$ and to achieve different material properties, see Table 2. Despite the comparable microscopic first-order hyperpolarizability, the macroscopic nonlinearity of JRD1 of $r_{33,JRD1}$ = 343 pm/V [28] exceed the values of DLD164 $r_{33,DLD164}$ = 137 pm/V [58], where both values have been measured at 1310 nm. Jin *et al.* demonstrated in [28] that a benzocyclobutene barrier can increase the bulk EO coefficients of monolithic organic EO materials up to $r_{33,JRD1}$ = 556 pm/V. However, application of a BCB charge blocking layer in plasmonic devices is hampered by the nanoscale feature sizes and layer thicknesses.

The two investigated organic EO materials are based on the commonly used amine donor – π bridge – tricyanofuran acceptor motif used in the well-studied organic EO chromophore YLD124 [21], see Fig. 3(c). The modification to create JRD1 introduces two sterically bulky *tert*-butyldiphenylsilyl (TBDPS) functional groups (red). This modification results in a chromophore that is amorphous, has good film-forming properties, and can be efficiently aligned even as a monolithic, high number density ρ_N material without a polymer host. Through a combined experimental and theoretical effort it has been established that the TBDPS groups provide enhanced molecular mobility such that even though the molecular dipole moment μ, and hyperpolarizability β, are comparable to chromophores like YLD124,

JRD1 can achieve a larger acentric order $\cos^3 \theta$ during electric field poling [28, 72] giving rise to a larger EO activity.

DLD164 [58] has an analogous donor – π bridge –acceptor structure, but with two modifications: a simple hexyl chain is attached on the donor end for improved solubility, and two alkylbenzoylcoumarin units are attached on the bridge ring. The coumarin-containing units impart good film-forming properties, producing monolithic films that do not crystallize, and have been shown in a similar chromophore system [67, 73, 74] to have long-range intermolecular cooperativity reducing the rotational degrees of freedom of the NLO portion of the molecule resulting in increased $\cos^3 \theta$ in spite of the decreased ρ_N.

The difference of the chromophores structure not only influences the achieved EO coefficients, but also the refractive index n' and the absorption n'' of the materials, see Fig. 4. While both materials feature a comparable real part of the refractive index in the telecommunication wavelength range (1310 nm, 1550 nm). JRD1 has a slightly larger imaginary part of the refractive index than DLD164. However, in the telecom wavelengths range the imaginary part of the refractive index and therefore the absorption of both materials is negligible.
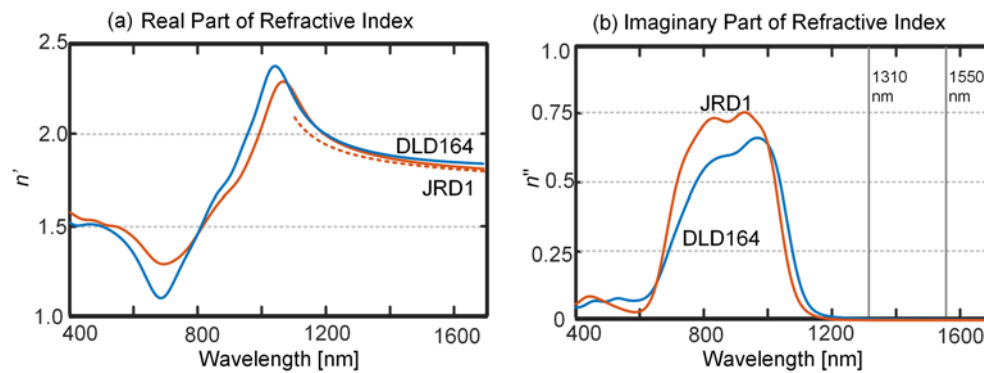

Fig. 4. Refractive indices of JRD1 [28] and DLD164 [58] measured by ellipsometry. (a) Real part: At the telecommunication wavelength of 1550 nm JRD1 features a comparable refractive index to DLD164 ($n_{JRD1}(1550 \text{ nm}) = 1.81$, $n_{DLD164}(1550 \text{ nm}) = 1.83$). (b) Imaginary part. At the communication wavelengths of 1310 nm and 1550 nm both materials offer a negligible imaginary part of the refractive index.

Table 2. Material properties of the organic EO materials JRD1, DLD164 and YLD124

	ρ_N [chromophores/nm^3]	best $r_{33,bulk}$ [pm /V] 1310 nm	Best $r_{33,in\text{-}device}$ [pm /V] 1550 nm	n 1310 nm / 1550 nm
JRD1 [28][this work]	0.533	343 / 556[a]	193[b]	1.87 / 1.81
DLD164 [43,58]	0.395	137[c]	180	1.9 / 1.83
YLD124 [28]	0.683	118 / 242[a]	-	2.0 / 1.9
25%YLD124/PMMA [43,58]	0.172	118	30	1.6 / 1.58
25%YLD124/PSLD41 [34,44]	-	285	230	1.77 / 1.73

[a] with charge blocking layer. [b] measured at 1600 nm, larger r_{33} is expected at lower wavelengths. [c] dielectric breakdown occurred during electric-field poling of bulk references limiting the maximum achievable r_{33}

Table 2 summarizes the material properties of above discussed monolithic organic EO materials JRD1, DLD164 as well as an example for a guest-host polymer system of 25 wt% YLD124 doped into 75 wt% PMMA. Neat YLD124 offers the highest chromophore density $\rho_{N,YLD124}$ which corresponds to 0.683 chromophores/nm^3, when doped into PMMA this number reduces to 0.172 chromophores/nm^3. While neat YLD124 has a higher chromophore density than DLD164 and JRD1, the latter two chromophores that have been optimized for a high loading factor $\rho_N \cos^3 \theta$, offer higher macroscopic EO coefficients. The two materials

benefit from an increased $\cos^3 \theta$ achieved with the help of the additional side chains. The coupling of $\rho_N \cos^3 \theta$ can be discussed more precisely by comparing the achieved bulk EO coefficients of 118 pm/V for the monolithic YLD124 and for the composite 25%YLD124/75% PMMA. When YLD124 is doped into PMMA to reduce chromophore-chromophore interaction ρ_N is decreased by a factor of 4, however, the EO coefficient stays the same. Due to the larger chromophore distance $\cos^3 \theta$ increases and fully compensates for the reduced ρ_N. When a charge blocking layer is present $\cos^3 \theta$ can be increased further resulting in even higher EO coefficients [28].

2.3. Decreased electro-optic coefficients in nanoscale geometries

The slot width dependent EO coefficient described in Section 2.1 can be connected to a slot width dependent loading parameter $\rho_N \cos^3 \theta$, see Eq. (1) in Section 2.2. In this section, we discuss possible effects reducing $\rho_N \cos^3 \theta$ in plasmonic slot waveguides. We attribute the observed reduction of the EO coefficient to a combination of the below mentioned effects.

2.3.a Slot filling effects

In very narrow slots the nonlinear material may not fill the complete slot area homogeneously. In 50 nm wide slots only approximately 20 to 30 molecules can align head-to-tail (chromophore length: ~2 nm from donor to acceptor). The constant bulk phase intrinsic number density ρ_N according to Table 2 cannot be assumed any more. Minor contaminants or other residuals as well as incomplete filling of only a few molecules can dramatically reduce the effective number density in the slot ρ_{slot}, so that in narrow slots: $\rho_N > \rho_{slot}$. Consequently, the EO coefficient in narrow slot devices is decreased compared to the materials bulk value: $\rho_N \cos^3 \theta \propto r_{33,bulk} > r_{33,dev} \propto \rho_{slot} \cos^3 \theta$.

2.3.b Surface effects

Surface interactions between the organic EO molecules and the slot sidewalls (Au, in the case of plasmonic slot waveguides, Si or SiO_2 in case of the silicon-organic hybrid waveguides) may lead to weak, noncovalent bonding that counteracts the ordering force induced by the poling field. Depending on the chemical structure of the organic EO molecule it aligns in a preferred orientation along the sidewalls [56, 62, 75]. Therefore, molecules in the vicinity of the interface have their motion restricted by the fixed surface and do not efficiently align with the poling field, resulting in a reduction of $\cos^3 \theta$ and thus in a reduced $r_{33,dev} \propto \rho_{slot} \cos^3 \theta$. In narrow slots the proportion of molecules being influenced by surface effects is large.

To further investigate this hypothesis, coarse-grained Monte-Carlo computer simulations of CLD-type chromophores filling a 5 nm × 5 nm electrode area of a plasmonic slot with widths ranging from 5 nm to 200 nm were performed under poling conditions ($E_{poling} = 100 \, \text{V}/\mu\text{m}$). We used the LoD coarse-graining method [76] and a model of the chromophore core previously published in [77]. Additional information, including the wall interaction potential, can be found in the Appendix A.1. The results of these simulations are displayed in Fig. 5. A strong decrease in the overall chromophore loading, $\rho_N \cos^3 \theta$, can be observed for plasmonic slot widths below 50 nm, see Fig. 5(a). Above a plasmonic slot width of 50 nm, the system asymptotes to the chromophore loading value obtained for bulk simulations of about $1.2 \cdot 10^{20}$ molecules/cm^3. The primary driving factor for the decrease in chromophore loading in narrower slots is the reduced overall acentric order, since the average density does not change. The acentric order is strongly affected by surface interactions between the EO molecules and the sidewalls. This is evidenced in Fig. 5(b), showing decreased acentric order for smaller slot widths due to strong average centrosymmetric order ($P_2 < 0$) perpendicular to the poling direction. While $P_2 = 0$ indicates the absence of

centrosymmetric order, $P_2 > 0$ signifies centrosymmetric order parallel to the poling direction. $P_2 < 0$ indicates a centrosymmetric order perpendicular to the poling direction. The negative centrosymmetric order parameter reflects the morphology near the gold (Au) surface: the molecules are aligning parallel to the Au surface. This is highlighted in Fig. 5(c), where a simulation-snapshot of the poled chromophore system is depicted. At the electrodes, molecules cannot penetrate into the Au layer, but must lie on the Au surface with their dipole moments predominantly ordered parallel to the surface. In contrast, in the bulk-region between the two Au surfaces the average molecule orientation points along the direction of the poling field. The simulations reveal the discrepancy between the bulk- and the surface-region in terms of the molecular order of the EO material.

Furthermore, in Fig. 5(b) it is interesting to note that the centrosymmetric order is increased by the presence of interfaces in comparison to bulk simulations [77], underlining the importance of surface interactions particularly for smaller systems.
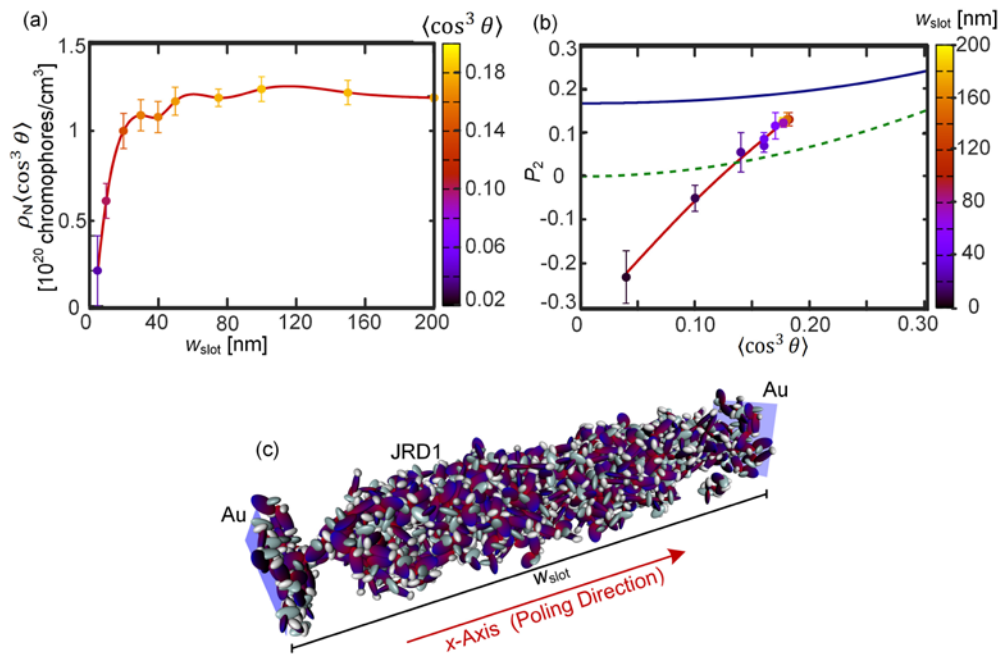

Fig. 5. (a) Simulated chromophore loading as a function of the plasmonic slot width. The achieved average acentric order $\cos^2 \theta$ is marked as the color of the data points. (b) Simulated centrosymmetric order, $P_2 = (3\cos^2 \theta - 1)/2$, in the poling direction as a function of the average acentric order, $\cos^2 \theta$, the plasmonic slot width is marked as the color of the data points. Additionally included are the centrosymmetric order parameters $P_2(\theta)$, is plotted as a function of the acentric order parameter $\cos^2 \theta$, obtained from Langevin theory for two-dimensional (blue, solid line) and three-dimensional (green, dashed line) dipole order orientational spaces in the independent particle limit. (c) Snapshot of a poled chromophore system in a 30 nm wide plasmonic slot.

2.3.c Inhomogeneous field distribution

Every microfabrication patterning method results in sidewalls that are not perfectly vertical and have some surface roughness, and the effects are more magnified when the dimensions are smaller. Waveguide inhomogeneity and the roughness of the waveguide sidewalls have a strong influence on the electric field distribution in the slot. During the poling process the alignment of the molecules roughly obeys $\cos^3 \theta \propto E_{\text{poling}}$ [78]. An inhomogeneous field

distribution during poling leads to an inhomogeneous and inefficient ordering of the molecules, thus reducing $\cos^3 \theta$. The influence of surface roughness is stronger in narrow slot.

2.3.d Current effects

A reduction of the slot width might lead to an increased electrical conductance G and thus to higher currents during poling:

$$I_{\text{poling}} = U_{\text{poling}} G_{\text{slot}} = U_{\text{poling}} \sigma_{\text{slot}} \frac{h_{\text{Au}} L_{\text{dev}}}{w_{\text{slot}}} \qquad (2)$$

where the conductance is defined by the conductivity of the material in the slot σ_{slot}, the cross sectional area $h_{\text{Au}} L_{\text{dev}}$ and the slot width w_{slot}. When the electrical power during poling is set to be constant, the higher current reduces the applied voltage and therefore reduces the poling field. When the power is not set to be constant, high currents may occur during poling, degenerating or destroying the organic EO material in the slot. During poling, however, a certain poling field $E_{\text{poling}} = U_{\text{poling}} / w_{\text{slot}}$ is desired. Therefore, a reduction of w_{slot} results in a reduction of U_{poling} in order to keep I_{poling} constant at decreased slot width. However, Zhang *et al.* [29] observe that the increased poling currents in narrow slots limit the poling efficiency of the organic EO material SEO125 [52]. In contrast to other studies [28, 29, 45], we did not observe a correlation between the EO coefficient and the poling current. Figure 6(a) depicts the maximum measured poling currents for different poling experiments of JRD1 as a function of the slot width. The achieved EO coefficients are color-coded. It can be seen from our plot, that narrow slots do not feature a remarkably larger poling current over devices with larger slot widths.
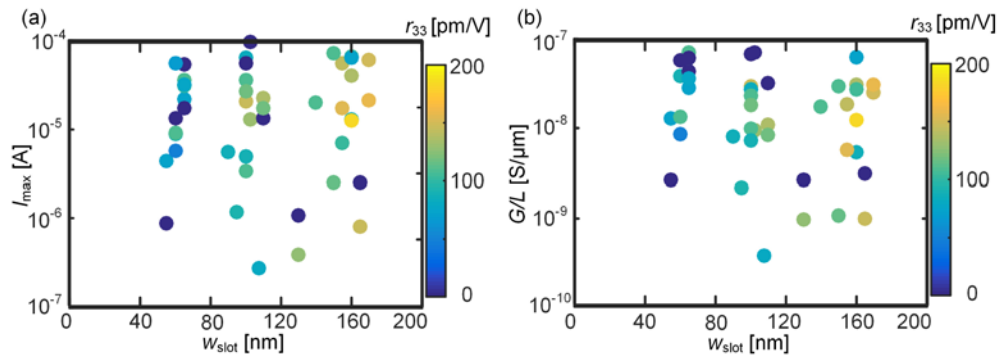

Fig. 6. (a) Maximum measured current during the poling process of JRD1 as a function of the plasmonic slot width. The achieved EO coefficient is marked as the color of the data points. (b) Maximum conductance G of JRD1 as a function of the plasmonic slot width measured above the glass transition temperature T_{g}. To take different device lengths into account, the conductance is normalized to the device length L. The achieved EO coefficient is marked as the color of the data points. No correlation between the EO coefficient, the current and the conductance is found. Narrow slots neither feature an increased maximum poling current nor lead to an increased material conductivity or increased charge injection.

Figure 6(b) depicts the corresponding normalized conductance $G/L = I_{\text{poling}} / \left(U_{\text{poling}} L_{\text{dev}} \right)$.

The conductance is normalized to L to take into account different device lengths. Here, one might see how the conductance decreases for wider slots, see Eq. (2), however there is no correlation between G/L and the EO coefficient r_{33}. The maximum achievable EO coefficient of JRD1 may be limited by another factor. The maximum applicable poling field for JRD1 was found to be in the order of ~180 V/µm. For larger applied fields the material in the slot suffers from dielectric breakdown. As a solution it has been suggested to overcome dielectric

breakdowns by preventing the effect with a charge blocking layer [28]. A blocking layer may also reduce surface effects of the chromophores described in Section 2.3.b.

2.3.e Underestimation of r_{33}

A proper simulation of the static and the optical electrical field distribution in the slot is important for deriving the values of the EO coefficients r_{33}. As will be mentioned in Section 3.1 and further described in the Appendix A.3, the EO coefficient cannot be measured directly. It can be calculated knowing the modulators device dimensions, its $U_{\pi}L$ product, and the simulated electric field distributions [40]. Variations from the simulated geometry strongly influence the calculated values of r_{33}. There are two effects that influence the simulated values. First, there are surface roughness and width variations along the waveguide that are difficult to include in a simulation and are therefore excluded. Surface roughness effects may lead to a slot-width effect. Second, there are non-vertical sidewalls that decrease the overall efficiency of a modulator. We have included non-vertical sidewalls by performing simulations with sidewalls at an angle of 5°. This value is a rather conservative number. Several devices have been cross-sectioned and imaged by SEM indicating a larger angle. This would mean that the nonlinear interaction in the slot-waveguide is less efficient than assumed, which means that the electro-optic coefficient r_{33} of the material is higher then what is estimated by assuming the moderate angle of 5° (see Appendix A.3). It can be seen how the angle dependence of the plasmonic slot waveguides has an effect on the overall value of the EO coefficient (~20%) but does not influence the slot-width dependence, see Appendix A.3.

3. In-device application: optimizing the plasmonic modulator performance

While optimizing a geometry for the largest possible EO coefficient might look like a reasonable choice, the overall performance of a device depends on more factors. For instance, for a real device it is not the EO coefficient that matters but the operation voltage and the losses. The operation voltage depends on the slot width and the length of the device. Naturally, the operation voltage will go down with length and for narrower slot widths. Unfortunately, longer length and narrower slot come at the expense of higher losses; therefore, we must optimize the factors for a particular application. Subsequently, we will discuss the overall optimum geometry of a modulator.

3.1. Plasmonic Mach-Zehnder modulators

The in-device performance of the organic EO materials was investigated with plasmonic Mach-Zehnder modulators (MZM) [36, 53] that have been fabricated in-house. We selected the POH device approach because they operate with some of the highest light matter interactions [40]. The combination of the organic EO material JRD1 with the plasmonic modulators allowed us to operate the devices from the on- to the off-state with small voltages of $U_{\pi} = 1.4$ V. Figure 7(a) depicts a colorized microscope picture of a plasmonic MZM. It consists of a silicon Mach-Zehnder interferometer with plasmonic phase modulators (PPMs) [35] in each arm, separated by the signal (S) electrode. Figure 7(b) shows a colorized scanning electron microscope (SEM) picture of a PPM. The PPM is formed by a metal-insulator-metal (MIM) slot waveguide filled with an organic EO material. The modulators were fabricated in-house as described in the Appendix A.2. They feature 200 nm high Au electrodes, device lengths L ranging from 12.5 µm to 75 µm and were fabricated with slot widths w_{slot} from 40 nm to 170 nm. In this slot-width range we expect high field confinement, reasonable propagation losses and a good overall modulator performance. For larger slot widths the MIM modes would lose the attractive characteristics of the strong MIM confinement. An in-detail discussion of the slot-width dependence of the guided plasmonic MIM modes can be found in [38].

The slots of the PPMs are filled with the nonlinear optical material, the organic EO material JRD1 [28] which was applied by spin coating. To induce the macroscopic second-

order nonlinearity in the material, the material must be poled. Therefore, after device fabrication, the organic EO material was poled near the material's glass transition temperature. In case of the plasmonic MZM this is performed according to, Fig. 7(c). A voltage is applied between the two outer electrodes of the modulator while the material is heated close to its glass transition temperature. The molecules align in response to the poling field (red arrows), E_p. The resulting average acentric order $\cos^3 \theta$ of the chromophores in the direction of the applied poling field gives rise to the bulk EO activity, see Section 2.2.
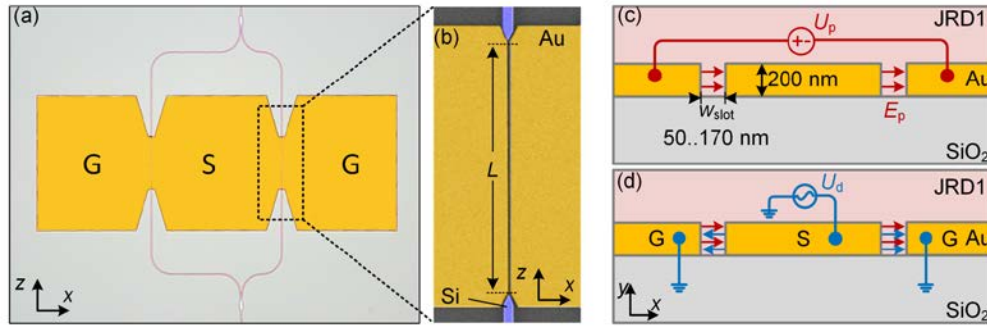

Fig. 7. (a) Colorized microscope picture of a plasmonic Mach-Zehnder modulator. (b) Colorized SEM picture of a plasmonic phase modulator. Light is guided in a plasmonic slot waveguide between two Au electrodes (c, d) Schematic and cross-sectional view into a plasmonic Mach-Zehnder modulator with fields applied for (c) device poling and (d) device operation.

To operate the MZM an electrical driving signal is applied to the signal electrode, Fig. 7(d). The voltage drops across the nanoscale slots of the PPMs. The field (blue arrows) in one PPM points in the same direction as the poling direction (red arrows) and opposite in the other PPM. This way, the phase changes induced by the linear EO effect in the two PPMs have equal magnitude but opposite signs. The intensity transfer function of a plasmonic MZM is given by

$$\left| \frac{E_{out}(U_d)}{E_{in}} \right|^2 \propto \frac{1}{2} \left(1 + \cos\left(\frac{4\pi}{\lambda_{OC}} \Delta n_{eff}(U_d) L - \Phi_{bias} \right) \right) = \frac{1}{2} \left(1 + \cos\left(\frac{4\pi}{\lambda_{OC}} \Gamma \frac{\Delta n_{mat}(U_d)}{n_{mat}} n_{slow} L - \Phi_{bias} \right) \right) \quad (3)$$

The transfer function follows a cosine function and its value changes with the relative effective refractive index change Δn_{eff}. The operation point can be adjusted by a phase offset Φ_{bias} either by applying a bias voltage, or, in case of an imbalanced MZI, by adjusting the wavelength. The effective refractive index change in the PPMs is directly proportional to the relative refractive index change $\Delta n_{mat}/n_{mat}$ induced by the Pockels effect. Furthermore, it scales with the waveguide dependent parameters n_{slow} and Γ [36, 40], as well as the PPM length L. The refractive index change Δn_{mat} depends linearly on the driving voltage U_d and the EO coefficient r_{33}

$$\Delta n_{mat} = -1/2 \cdot r_{33} n_{mat}^3 U_d / w_{slot} . \quad (4)$$

The influence of the material on the modulator drive voltage and required modulator length can be assessed using the expression for the voltage-length product derived in the Appendix A.3

$$U_\pi L = \frac{\lambda_{OC}}{2} \cdot \underbrace{\frac{w_{slot}}{\Gamma n_{slow}}}_{\text{waveguide}} \cdot \underbrace{\frac{1}{r_{33} n_{mat}^2}}_{\text{OEO material}} . \quad (5)$$

Equation (5) emphasizes the importance of the organic EO material. The $U_\pi L$ product inversely scales with the EO coefficient. Therefore, an organic EO material with a high r_{33} is desirable for lowest driving voltages. In addition, the nonlinear interaction geometry of the waveguide can be maximized to enhance the influence of the Pockels effect on $U_\pi L$. This can be achieved by maximizing the waveguides dependent parameters Γn_{slow} [40] and reducing the w_{slot} waveguide width, as discussed in detail in Section 3.2 and in Refs [36, 40].

To measure the in-device EO coefficient, a laser ($\lambda \approx 1600$ nm) was coupled to the device and a triangular low-frequency electrical driving signal was applied to the modulator, Fig. 8(a). The modulated optical output signal was detected with a photodiode and evaluated on an oscilloscope. The modulated intensity follows the transfer function Eq. (3). For a drive signal with a peak-peak voltage of $U_d = U_\pi = U_{off} - U_{on}$ the intensity follows a cosine. For $U_d > U_\pi$ the intensity signal is over modulated and U_π can easily be determined by relating the maximum and minimum of the optical signal to the corresponding voltages. Figure 8(b) depicts a measured, over-modulated intensity signal (red) of a MZM ($L = 50$ µm, $w_{slot} = 60$ nm) for an applied electrical triangular signal (blue) with $U_d = 3$ V_{pp}. From the plot one can derive an on-off voltage that is as small as $U_\pi = 1.4$ V_{pp}. Knowing U_π, one can calculate r_{33} using simulated values for Δn_{eff} [36]. The values of Δn_{eff} were obtained by performing simulations as described within [40]. For getting the proper values, waveguide dimensions were adapted and non-vertical sidewalls were included, see Appendix A.3.
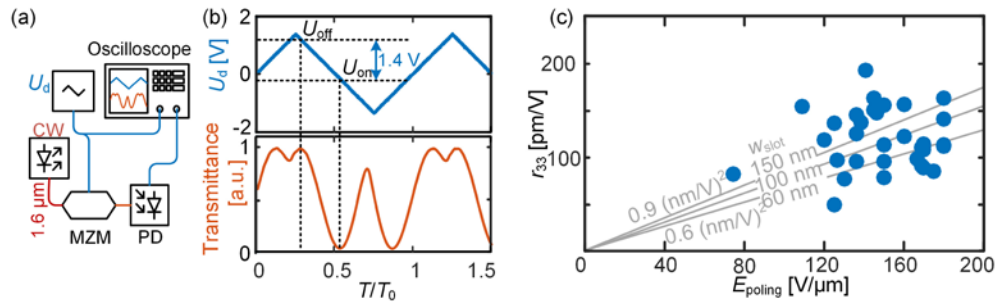

Fig. 8. (a) Schematic of the characterization setup. (b) Triangular voltage sweep and corresponding intensity modulation with $U_d > U_\pi = 1.4$ V. (c) EO coefficient r_{33} as a function of the poling field. The poling efficiency r_{33}/E_{poling} is plotted for different slot widths and shows a strong slot width dependence. The JRD1 material provides EO coefficients up to $r_{33,max} = 193$ pm/V.

Figure 8(c) depicts the measured EO coefficients of JRD1 as a function of the poling field. It can be seen that EO coefficients of up to $r_{33,max} = 193$ pm/V are found.

Figure 8(c) further shows a strong dependence of the poling efficiency (PE) r_{33}/E_{poling} on the plasmonic slot width. While we found for widest slots ($w_{slot} \approx 150$ nm) an average PE of 0.9 $(nm/V)^2$ with $r_{33,max} = 193$ pm/V, we found for narrower slots reduced values. E.g. for slot widths of 100 nm we found a PE of 0.8 $(nm/V)^2$ with $r_{33,max} = 156$ pm/V and for slot widths of 60 nm a PE of 0.6 $(nm/V)^2$ with $r_{33,max} = 137$ pm/V. For wide slots, the measured in-device EO coefficients are in good agreement to what is found in bulk materials (w/o charge blocking layers) [28]. Note that bulk measurements were performed at $\lambda = 1310$ nm [28] while the in-device characterization was performed at $\lambda \approx 1600$ nm. Larger in-device EO coefficients are expected at shorter wavelengths [45, 62] closer to the material absorption peak around 900 nm. The observed variations of the measured EO coefficients are comparable to what was observed in bulk measurements [28]. We attribute them to variations of the film and waveguide quality.
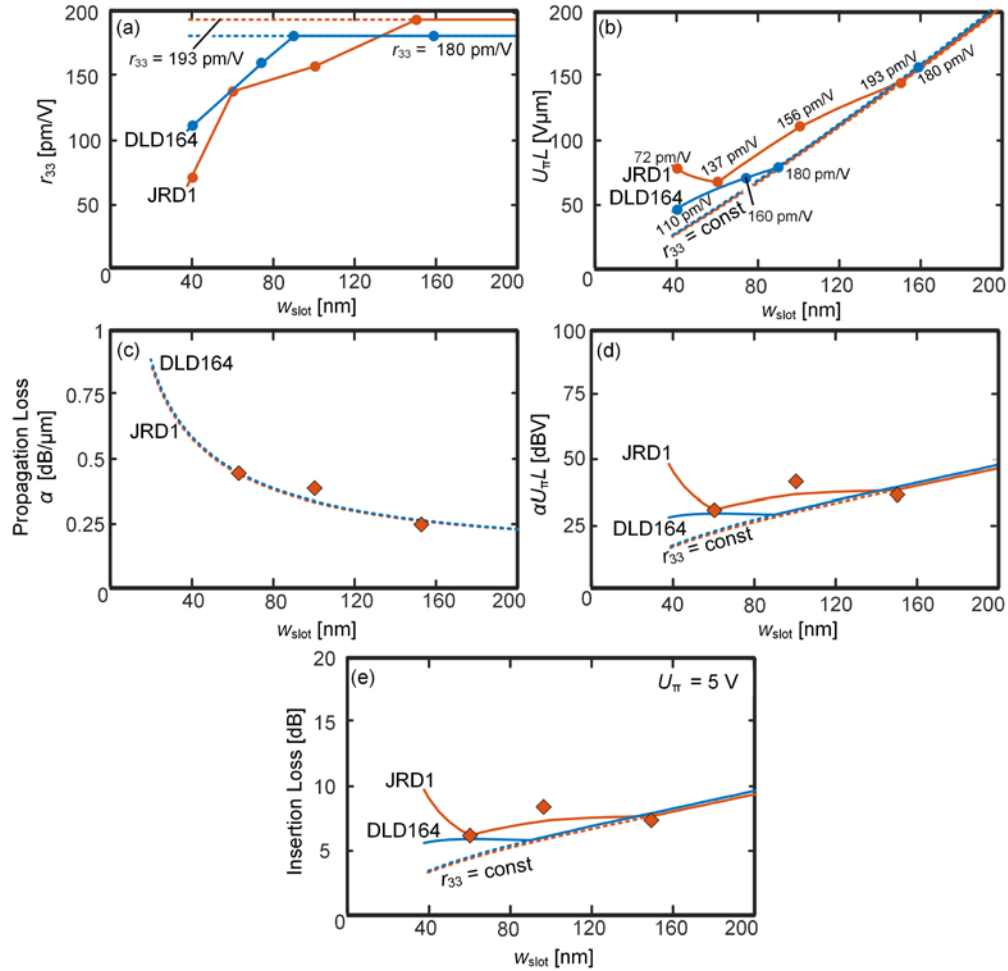
3.2. Optimizing the modulator performance

Fig. 9. (a) Measured EO coefficients r_{33} as a function of the slot width for JRD1 and DLD164 (solid lines) and ideal case with a constant r_{33} (dashed lines). (b) $U_\pi L$ for devices with different slot widths. The solid lines show the experimental values, the dashed line indicates the ideal $U_\pi L$ if r_{33} coefficients were constant across all slot widths. (c) Plasmonic propagation losses α derived from theory (dashed lines) for the two nonlinear materials and extracted from cut-back measurements (diamonds) for JRD1. The plasmonic losses are comparable for the two materials because they have a similar refractive index. (d) $\alpha U_\pi L$ figure-of-merit for measured (solid) and ideal (dashed) EO coefficients. The lines are calculated using simulated values of α, diamonds represent $\alpha U_\pi L$ for measured propagation. (e) Expected modulator insertion loss for a MZM when the modulator length is adapted to maintain $U_\pi = 5$ V. The plots show loss values for the measured r_{33} from above (solid) and the expected losses if r_{33} would be ideal (dashed). The diamonds show the insertion loss for measured propagation losses.

The slot width dependence of the EO coefficient r_{33} discussed in Sections 2.1 and 3.1 strongly affects the performance of any Pockels effect based MZM. In the case of the plasmonic MZMs, this slot width dependence has to be taken into account, when assessing the influence of the slot width on device parameters such as the $U_\pi L$ product and the insertion loss. Here, we investigate these influences for the materials DLD164 and JRD1 on POH MZMs, compare the two materials, and find optimum waveguide widths for low-loss modulators.

The $U_\pi L$ products for JRD1 and DLD164 are shown in Fig. 9(b). In the ideal case (dashed lines), $U_\pi L$ would decrease nearly linearly with a decreasing slot width. Despite the slightly

lower $r_{33,\text{max}}$ of DLD164 compared to JRD1, the $U_\pi L$ of DLD164 is comparable to that of JRD1. This originates in the refractive index dependence of the Pockels effect. The index change Δn_{mat} depends on r_{33}, but also goes with the cube of the refractive index n^3_{mat}, see Eq. (4). The higher refractive index of DLD164 (see Fig. 4) results in a comparable $n^3 r_{33}$ value – a common figure of merit (FOM) to assess the EO coefficients. The FOM calculates to $1.83^3 \cdot 180$ pm/V = 1103 pm/V for DLD164 and to $1.805^3 \cdot 193$ pm/V = 1135 pm/V for JRD1, respectively. This explains the comparable $U_\pi L$ products for the two materials. When going to narrower slots, the theory would predict a nonlinear interaction enhancement that scales with $1/w_{\text{slot}}$ [40]. However, when taking into account the slot width dependence of r_{33}, $U_\pi L$ flattens for narrowest slots. Yet, the $U_\pi L$ product of DLD164 still improves for values down to 40 nm. At narrowest slot widths DLD164 then offers a lower $U_\pi L$ product than JRD1. For both materials, JRD1 and DLD164 the smallest $U_\pi L$ values are found at narrow slow widths, offering values below 70 Vµm and 50 Vµm, respectively.

Another important parameter is the overall propagation loss in plasmonic modulators. Unfortunately, when reducing the slot width, not only does $U_\pi L$ deviate from linearity, but also the plasmonic propagation loss in the slot waveguide increases [36, 40]. Figure 9(c) depicts the propagation losses as a function of the slot width. The similar refractive indices of the materials lead to comparable propagation losses α, Fig. 9(c) where JRD1 features a slightly lower plasmonic propagation loss. To experimentally verify the plasmonic propagation loss, we performed cut-back measurements using modulators filled with JRD1 with lengths of 12.5 to 75 µm and slot widths of 60 nm, 100 nm, and 150 nm. We found plasmonic propagation losses of approximately 0.45 dB/µm, 0.38 dB/µm, and 0.25 dB/µm, respectively. These measurements are included in Fig. 9(c) as diamonds. The propagation loss can be related to the total plasmonic in-device losses. A useful FOM to evaluate the in-device loss for a given π-voltage is the product of $U_\pi L$ and the propagation loss α [25], Fig. 9(d). The $\alpha U_\pi L$ FOM gives the π-voltage of a modulator with an insertion loss of 1 dB, or the insertion loss αL of a modulator for a fixed π-voltage $U_{\pi,\text{fix}}$: $\alpha L = \alpha U_\pi L / U_{\pi,\text{fix}}$. The insertion loss αL is plotted in Fig. 9(e) as a function of the slot width. In all cases the device length was adapted to maintain a $U_{\pi,\text{fix}} = 5$ V. If the EO coefficients were ideal, i.e. constant for all slot-widths (dashed line), the slightly higher $n^3 r_{33,\text{const}}$ FOM of JRD1 as well as the lower plasmonic propagation losses would lead to slightly lower overall losses when using JRD1. For a given EO coefficient the nonlinear interaction increases with decreasing slot width [40]. This in turn allows for shorter devices, compensating the high propagation loss in narrow slots. The insertion losses would converge towards 0 dB. Yet, the EO coefficient decreases with decreasing slot width. Compared to the ideal case, modulators need to be longer to achieve the same π-voltage resulting in higher insertion loss. Thus, there is an optimum slot width where total loss and required electrical drive voltage are in a balance. For JRD1 we find lowest losses for slot widths around 60 nm corresponding to minimum plasmonic losses of 6 dB for lengths in the order of 15 µm. Reducing the slot width further would increase the insertion loss again. DLD164 however, can benefit from the higher $n^3 r_{33}$ FOM at narrow slots and therefore theoretically result in a lowest insertion loss down to 40 nm. Fabrication of such narrow slots however is challenging [36] and sidewall roughness might increase the propagation losses. At the slot width of ~75 nm—where phase modulator fabrication is still quite reproducible [36]—both materials show good performance and do not suffer significantly from slot width dependent performance penalties.

4. Conclusion

We have investigated the electro-optical activity of organic EO materials in narrow plasmonic slot waveguides. EO coefficients of up to 193 pm/V (measured at 1600 nm) were found. Furthermore, it has been found that the electro-optic coefficient decreases with the slot width. The large EO coefficient reduces to values in the order of 140 pm/V for slot widths below 80 nm. Possible reasons for this reduction have been discussed. It has been confirmed by Monte-

Carlo simulations, that chromophore-surface interactions are an important factor reducing the electro-optic coefficient in narrow plasmonic slots.

We have further investigated the influence of the slot-width dependent EO coefficient on the performance of plasmonic modulators. Fortunately, the sub-diffraction light confinement in plasmonic slot waveguides leads to an enhanced nonlinear interaction [40]. This enhanced nonlinear interaction can in part compensate for the observed reduction of the EO coefficient in narrow slots. In detail, we discuss the influence of the slot width and the EO coefficient on the performance of the plasmonic-organic hybrid Mach-Zehnder modulators. In particular, the slot width dependence of the $U_\pi L$ product and the insertion loss of these modulators are investigated. Devices that require the lowest voltage-length product ideally come with slot widths in the order of 60 nm. It is shown that despite decreasing EO coefficients for narrow slots, the voltage-length product decreases for narrow slots to values on the order of 70 Vµm and 50 Vµm for the materials JRD1 and DLD164, respectively. Conversely, plasmonic modulators have lowest overall losses (on the order of 6 dB) for plasmonic waveguides with slot widths of 60 – 100 nm. In this slot-width range the POH modulators feature lowest losses and offer low drive voltages while being easy to fabricate with sufficient fabrication tolerance [36].

Finally, it was shown how the combination of the organic EO material JRD1 within a plasmonic-organic hybrid EO modulator has enabled the fabrication of a MZM device with on/off voltages as low as $U_\pi = 1.4$ V. Such low U_π have become possible by material and poling improvements and by improved fabrication processes that resulted in lower overall losses and thus enabled us to fabricate plasmonic devices with a length of 50 µm. This work demonstrates that the plasmonic modulator technology not only offers high-speed >170 GHz operation [37] and most-compact footprints [38] but can also offer low operation voltages in the order of 1 V.

Appendix

A.1 Monte-Carlo simulations

Simulations were performed using the isothermal-isobaric (NPT) ensemble with re-entrant conditions in the two directions perpendicular to the poling field. In this case, the system density in not proscribed in advance of the simulation. A pressure of 1 atm and a temperature of 400 K is assumed. In order to simulate two fixed walls located at $\pm L/2 \cdot \hat{e}_x$ along the poling direction (x-direction), volume moves as well as periodic boundary conditions were only applied in the y- and z-directions. The interaction potential of an ellipsoid with associated charges as well as dipoles with both surfaces includes van der Waals-type (vdW-type) and electrostatic interactions.

The vdW-type interaction of an ellipsoid at location $\bar{r}_i$ with a wall is calculated using a generalized, Gay-Berne-type, Lennard-Jones (LJ) potential:

$$V_{\text{wall}}\left(\bar{r}_i\right) = 4\sqrt{\varepsilon_{\text{wall}}\varepsilon_i}\left[\left(\frac{w_{\text{wall}} + w_i}{\left(\frac{L}{2} - \left|\left(\bar{r}_i\right)_x\right|\right) - \sigma_{\min,i} + \left(w_{\text{wall}} + w_i\right)}\right)^{12} - \left(\frac{w_{\text{wall}} + w_i}{\left(\frac{L}{2} - \left|\left(\bar{r}_i\right)_x\right|\right) - \sigma_{\min,i} + \left(w_{\text{wall}} + w_i\right)}\right)^6\right] \quad (6)$$

Here, $\varepsilon_{\text{wall}}$ and ε_i are the potential well depth contributions of the wall and ellipsoid, while w_{wall} and w_i are the width contributions of the wall and the ellipsoid, respectively. Note that due to using the absolute x-position of the ellipsoid, $\left|\left(\bar{r}_i\right)_x\right|$, and the inherent symmetry of the ellipsoid this potential calculates the interaction energy with walls at both

$\pm \dfrac{L}{2}\hat{e}_x$ locations. The minimum distance of contact between an ellipsoid and a plane, $\sigma_{\min,i}$, is provided in the literature [79].

The electrostatic potential energy follows our implemented method [76]. Additionally, we add potential energy contributions from image charges and image dipoles due to the (in general existing) mismatch between the dielectric constants between the bulk material and the interface material.

For the present simulations, the wall parameters have been estimated from the LJ parameters for Au [80]: $\varepsilon_{\text{wall}} = 5.29\,\text{kcal/mol}$, $w_{\text{wall}} = 2.63\,\text{Å}$, and a dielectric constant of 10^6 consistent with a conductive material has been used.

A.2 Device fabrication

As described in [36]: "The devices were fabricated in-house on a SOI wafer consisting of a 220 nm thick Si device layer and a 3 μm thick buried oxide. The structures were patterned by electron-beam lithography in a Vistec EBPG5200 system. A negative tone ebeam resist was used to pattern photonic components comprising waveguides, MMIs and fiber-to-chip GCs. The patterns were transferred into the Si device layer by applying a dry etching process. Plasmonic MIM waveguides and electrodes were produced with a lift-off process applied to a 200 nm thick e-beam evaporated Au layer."

A.3 Derivation of the EO coefficient r_{33} from measured voltage-length products

The EO coefficient r_{33} of a nonlinear material functionalized in a nanoscale slot cannot be measured directly. However, it can be determined by employing the measured voltage-length product $U_\pi L$ of a modulator [25, 40, 81]. An analytic expression for the EO coefficient can be derived by starting with the intensity transfer function of the plasmonic MZM [36]

$$\left|\frac{E_{\text{out}}(U_{\text{d}})}{E_{\text{in}}}\right|^2 \propto \frac{1}{2}\left(1 + \cos\left(\frac{4\pi}{\lambda_{\text{OC}}}\Delta n_{\text{eff}}(U_{\text{d}})L - \Phi_{\text{bias}}\right)\right) = \frac{1}{2}\left(1 + \cos\left(\frac{4\pi}{\lambda_{\text{OC}}}\Gamma\frac{\Delta n_{\text{mat}}(U_{\text{d}})}{n_{\text{mat}}}n_{\text{slow}}L - \Phi_{\text{bias}}\right)\right) \tag{7}$$

The transfer function in the on- and the off-state is given by

$$\text{on-state:}\ 1 = \frac{1}{2}\left(1 + \overbrace{\cos\left(\underbrace{\frac{4\pi}{\lambda_{\text{OC}}}\Delta n_{\text{eff}}(U_{\text{on}})L - \Phi_{\text{bias}}}_{0}\right)}^{=1}\right),$$

$$\text{off-state:}\ 0 = \frac{1}{2}\left(1 + \overbrace{\cos\left(\underbrace{\frac{4\pi}{\lambda_{\text{OC}}}\Delta n_{\text{eff}}(U_{\text{off}})L - \Phi_{\text{bias}}}_{=-1}\right)}^{\pm\pi}\right) \tag{8}$$

In the on- and the off-state of the modulator, the argument of the cosine needs to be 0 and $\pm\pi$, respectively. Assuming $\Phi_{\text{bias}} = 0$ the arguments simplify to

$$\text{on-state:}\ 0 = \left(\frac{4\pi}{\lambda_{\text{OC}}}\Delta n_{\text{eff}}(U_{\text{on}})L\right),$$

$$\text{off-state:}\ \pi = \frac{4\pi}{\lambda_{\text{OC}}}\Delta n_{\text{eff}}(U_{\text{off}})L = -\frac{2\pi}{w_{\text{slot}}\lambda_{\text{OC}}}\Gamma r_{33}n_{\text{mat}}^2 n_{\text{slow}}U_{\text{off}}L. \tag{9}$$

The voltages U_{on} and U_{off} calculate to

$$U_{\text{on}} = 0 \text{ V},$$

$$U_{\text{off}} = -\frac{\lambda_{\text{OC}}}{2} \cdot \frac{w_{\text{slot}}}{\Gamma n_{\text{slow}} L} \cdot \frac{1}{r_{33} n_{\text{mat}}^2}. \tag{10}$$

The voltage to switch the modulator from the on- to the off-state U_π and the voltage-length product $U_\pi L$ are then given by

$$U_\pi = U_{\text{on}} - U_{\text{off}} = \frac{\lambda_{\text{OC}}}{2} \cdot \frac{w_{\text{slot}}}{\Gamma n_{\text{slow}} L} \cdot \frac{1}{r_{33} n_{\text{mat}}^2},$$

$$U_\pi L = \frac{\lambda_{\text{OC}}}{2} \cdot \underbrace{\frac{w_{\text{slot}}}{\Gamma n_{\text{slow}}}}_{\text{waveguide}} \cdot \underbrace{\frac{1}{r_{33} n_{\text{mat}}^2}}_{\text{OEO material}}. \tag{11}$$

The expression for the EO coefficient is then found to be

$$r_{33,\text{max}} = \frac{\lambda_{\text{OC}}}{2 n_{\text{mat}}^2} \frac{w_{\text{slot}}}{U_\pi L} \frac{1}{\Gamma n_{\text{slow}}} \tag{12}$$

The function depends on measurable values such as the slot width w_{slot}, the wavelength of the optical carrier λ_{OC} and the material's refractive index n_{mat}. The two other quantities, namely the field energy-interaction factor Γ and the slowdown factor n_{slow}, need to be determined by means of simulations based on the measured slot height, slot width and the material dispersion of the metal (Au) and the OEO-material, see [40].

The geometry of the plasmonic slot is obtained from SEM images, as exemplarily shown in Fig. 10(a). Figure 10(b) shows a cross-section of a plasmonic slot waveguide. The Au sidewalls are not perfectly vertical but drop over tens of nanometers In this example sidewall-angles of approximately 10° to 15° are found. Non-vertical sidewalls strongly influence the field distribution in the plasmonic waveguide. This has a strong influence on the field-energy interaction factor Γ. Therefore, we adapted the theoretical framework of [40] as follows:
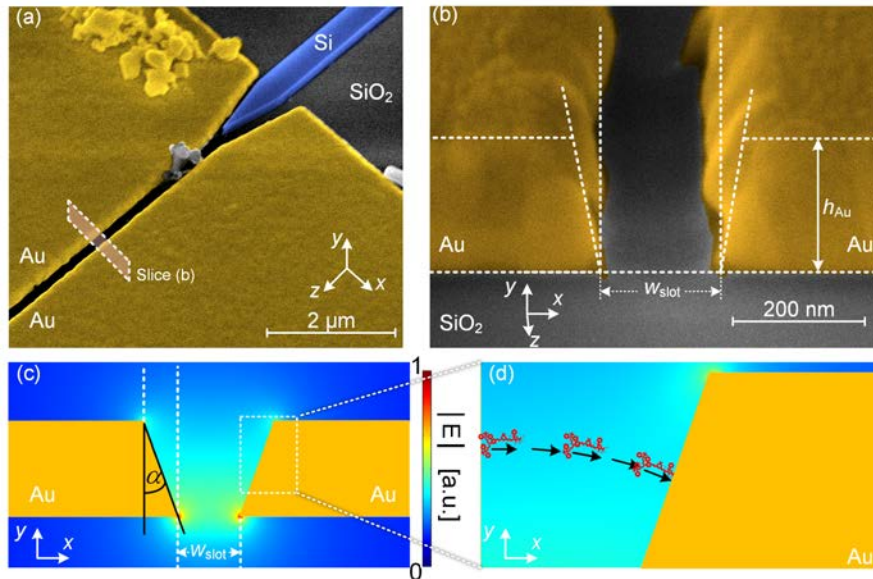

Fig. 10. (a) Colorized SEM image of a plasmonic slot waveguide and feeding silicon waveguide. (b) Cross section of a plasmonic slot waveguide with a sidewall angle of approximately 10° to 15°. Image was taken with an angle of 52°. (c) Cross section of slot with $\alpha = 10°$ and simulated poling field (color-coded) (d) In case of tilted sidewalls, chromophores may not be ordered parallel to x-axis

1. Non-vertical sidewalls result in an inhomogeneous field distribution of the poling-field E_{poling}, see Fig. 10(c). The amplitude of the electrical poling field is color-coded and is highest at the tip of the Au (lightning rod effect). Furthermore, the boundary condition requires the electrical field to be perpendicular to the Au surface. During electric field poling, the EO chromophores should align parallel to the electrical field. Thus the chromophores experience a position dependent rotation, see Fig. 10(d).

2. The EO coefficient r_{33} depends linearly on the applied poling field [28, 34, 58], and thus an inhomogeneous poling field results in an inhomogeneous EO coefficient $r_{33}(x,y)$ which needs to be considered. For instance, the maximum poling field appears at smallest distance between the two Au electrodes (Fig. 10(c).) resulting in the largest r_{33} at the bottom of the slot. To account for the inhomogeneous strength of the EO-coefficient we introduce the dimensionless weighting factor

$$\eta(x,y) = \frac{r_{33}(x,y)}{r_{33,\max}} \frac{\sqrt{E^2_{x,\text{poling}}(x,y) + E^2_{y,\text{poling}}(x,y)}}{\dfrac{U_{\text{poling}}}{w}} \tag{13}$$

3. The EO molecules are no longer oriented parallel to the substrate. Their orientation follows the poling field's direction as it can be seen in Fig. 10(d). In the center of the slot the molecular dipole axis $\bar{\mu}$ is parallel to the global coordinate system's x-axis, while angle of rotation β is largest at the Au surface. Therefore, the assumption that the light-matter interaction is expressed only by the x-component of the RF and optical fields may no longer be valid. The RF-field (RF) and optical field (OC) need to be mapped on the dipole axis $\bar{\mu}$ of the EO molecule ($E_{\hat{x},\text{RF}}(x,y) \; E_{\hat{x},\text{OC}}(x,y)$). We approximated the RF-field by the static poling field as $\lambda_{RF} \gg w_{\text{slot}}$. Therefore

$$E_{\hat{x},\text{RF}} \cong E_{\hat{x},\text{poling}} \sqrt{E^2_{x,\text{poling}}(x,y) + E^2_{y,\text{poling}}(x,y)}$$

4. To maintain the physical interpretation of the field-energy interaction factor Γ we normalize it by $U_{\text{poling}} / w_0 = E_{\text{poling,max}}$.

This leads to an adapted definition of the field-energy interaction for non-vertical sidewalls

$$\Gamma \cong \frac{\epsilon_r \iint\limits_{S_{\text{slot}}} (\eta^2(x,y) E^2_{\hat{x},\text{OC}}) d\sigma}{\iint\limits_{S} \left(\epsilon_0 \dfrac{d(\epsilon(\omega)\omega)}{d\omega} \mathbf{E}_{\text{OC}} \mathbf{E}^+_{\text{OC}} - \mu_0 \mathbf{H}_{\text{OC}} \mathbf{H}^+_{\text{OC}} \right) d\sigma} \tag{14}$$

Here, $\mathbf{E}^+ = E_x \hat{x} + E_y \hat{y} - E_z \hat{z}$ and $\mathbf{H}^+ = -H_x \hat{x} - H_y \hat{y} + H_z \hat{z}$ are representing the adjoint fields. The slow down factor is given by

$$n_{\text{slow}} = \frac{c_0}{v_{\text{energy}}} = c_0 \frac{\iint\limits_{S} \left(\epsilon_0 \dfrac{d(\epsilon(\omega)\omega)}{d\omega} \mathbf{E}_{\text{OC}} \mathbf{E}^+_{\text{OC}} - \mu_0 \mathbf{H}_{\text{OC}} \mathbf{H}^+_{\text{OC}} \right) d\sigma}{\iint\limits_{S} (\mathbf{E}_{\text{OC,t}} \times \mathbf{H}_{\text{OC,t}}) \cdot \hat{z} \, d\sigma} \tag{15}$$

The EO coefficient r_{33} obtained from Eq. (12) is the maximum value which can be found in the slot at the position where the poling field is largest. However, a fair comparison of the EO-coefficient of various materials requires an averaged coefficient. As the poling efficiency is linearly depending on the poling field we define the average EO-coefficient in the slot by

$$r_{33,\text{avg}} = r_{33,\text{max}} \cdot \frac{\text{mean}\left(E_{\text{poling}}\right)}{E_{\text{poling,max}}} \tag{16}$$

Adapting the method to calculate the EO coefficient r_{33} to non-vertical sidewalls and an inhomogeneous field distribution influences the resulting values. Table 3 summarizes the calculated EO coefficient r_{33} for different simulation assumptions. The method of a constant EO coefficient $r_{33,\text{const}}$ assumes perfectly vertical sidewalls and a constant electrical field in the slot [25, 43, 81, 82] ($E_{\text{poling,}} = U_{\text{poling}} / w_{\text{slot}}$). For wide slots, this method results in larger EO coefficients as the adapted method used in this work.

Table 3. EO coefficients r_{33} calculated for different calculation methods and simulation assumptions

w_{slot}	0° $r_{33,\text{const}}$	0° $r_{33,\text{avg}}$	5° $r_{33,\text{avg}}$	5° $r_{33,\text{max}}$	10° $r_{33,\text{avg}}$	15° $r_{33,\text{avg}}$
	[pm/V]	[pm/V]	[pm/V]	[pm/V]	[pm/V]	[pm/V]
40 nm	55	52	72	103	76	74
60 nm	112	104	137	176	150	152
100 nm	144	126	156	183	175	184
150 nm	199	163	193	215	215	230

In this paper, we assumed a sidewall angle of 5° (marked in grey). The maximum EO coefficients, $r_{33,\text{max}}$ is included for the angle of 5°.

Table 3 also summarizes the calculated EO coefficients for different sidewall angles. In this work we calculated the EO coefficient by assuming an sidewall angle of 5°. This value is a rather conservative number. Several devices have been cross-sectioned and imaged by SEM indicate a larger angle (see Fig. 10(b)) – which would mean that the nonlinear interaction in the slot-waveguide is less efficient than assumed – which means that the electro-optic coefficient r_{33} may be actually higher then what is estimated by assuming the moderate angle of 5°
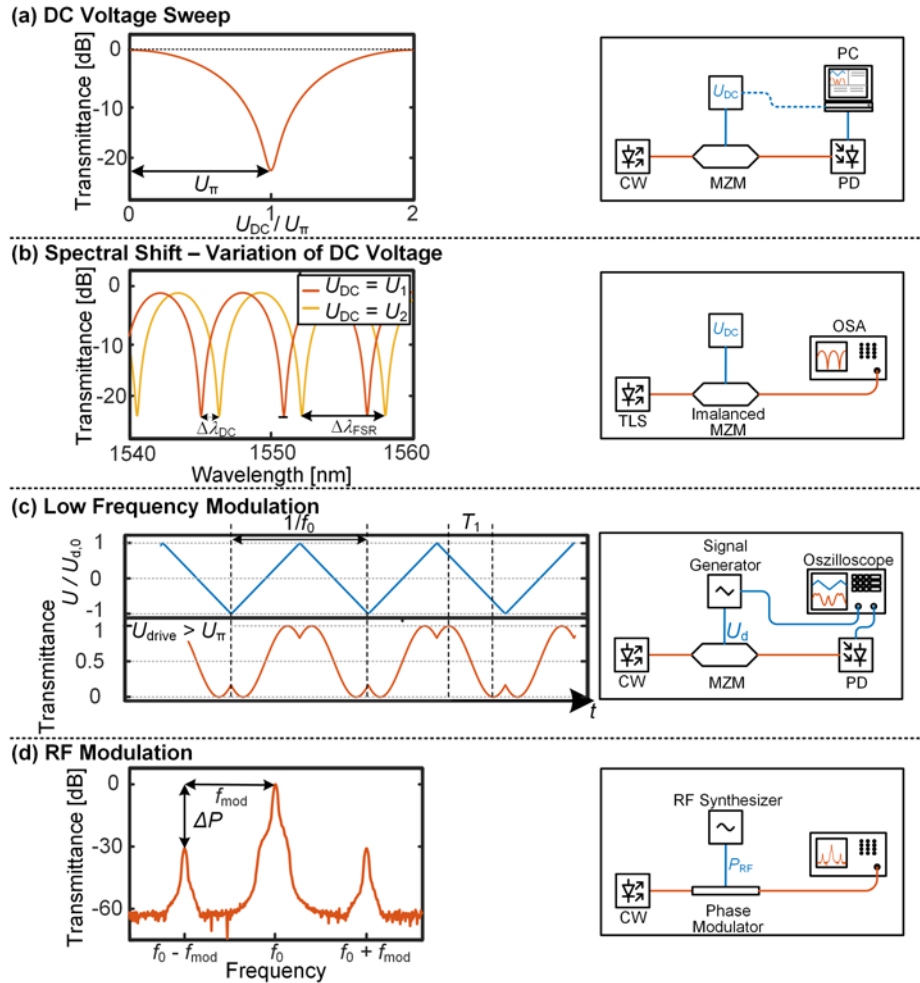
A.4 Measurement methods for U_π

Fig. 11. (a) Voltage sweep method to determine $U_\pi L$ of an MZM: U_π can be directly measured in the T vs. U plot. A CW laser is fed to the MZM while a DC voltage is applied to the monitor. The applied voltage and the modulator output power are recorded while the applied voltage is linearly increased. (b) Wavelength sweep method to determine $U_\pi L$ of an imbalanced MZM: The spectral shift can be measured and related to the applied DC voltage to calculate U_π. (c) Low frequency modulation method to determine $U_\pi L$ of an MZM: A triangular low-frequency drive signal is applied to the MZM. For $U_{drive} > U_\pi$ the modulated optical time signal shows signs of overmodulation. The on-off time T_1 can be related to the modulation frequency to calculate U_π. (d) RF modulation method to determine $U_\pi L$ of a phase modulator: A sinusoidal RF drive signal is applied to the phase modulator. The ratio between the optical carrier and the modulation

A.4.a DC voltage sweep

To measure the voltage dependent power transmission of a MZM as depicted in Fig. 11(a). A DC voltage is applied to the modulator while the transmitted power is monitored with a photodiode. The applied voltage is linearly increased and both the applied voltage and the transmitted power are recorded. U_π can be directly measured in the T/U plot if $\max(U_{DC}) > U_\pi$ [34, 36, 43]. Otherwise, U_π can be estimated by fitting the measured data with the expected transfer function [40].

A.4.b Wavelength sweep – variation of DC voltage

In case of an imbalanced MZM an applied optical voltage changes the optical transmission spectrum. To perform the measurement, a tunable laser source (TLS) is fed to the device while a defined voltage U_1 is applied to the modulator. The transmission spectrum is recorded using an optical spectrum analyzer (OSA) / power meter. The voltage is changed to U_2 and a second spectrum is recorded. Comparing the recorded spectra, a shift of the transmission spectrum by $\Delta\lambda_{DC}$ is observed, Fig. 11(b). Relating $\Delta\lambda_{DC}$, the free spectral range (FSR) $\Delta\lambda_{FSR}$ of the imbalanced MZI and the applied voltages, U_π can be calculated [53]

$$U_\pi = \frac{\Delta\lambda_{FSR} \cdot (U_2 - U_1)}{2\Delta\lambda_{DC}} \tag{17}$$

A.4.c Low frequency modulation

To measure U_π in the low frequency range a triangular low-frequency ($f = f_0$) drive signal is applied to the modulator [19, 45]. Light from a CW laser is fed to the modulator and the modulated signal is received by a photodetector. Drive signal and the modulated intensity are inspected by an oscilloscope, Fig. 11(c). The modulated intensity follows the modulator transfer function Eq. (3). For a drive signal with a peak-peak voltage of $U_d = 2\,U_{d,0} = U_\pi = U_{off} - U_{on}$ the intensity follows a cosine. For $U_d > U_\pi$ the intensity signal is overmodulated and U_π can easily be determined by relating the maximum and minimum of the optical signal to the corresponding voltages, Fig. 11(c).

$$\frac{1}{f_0} = T_0, \qquad \frac{T_1}{T_0/2} = \frac{U_\pi}{U_d}, \qquad U_\pi = \frac{T_1}{T_0/2} \cdot U_d \tag{18}$$

A.4.d RF modulation in plasmonic phase modulators

To assess the modulation efficiency of phase modulators the $U_{\pi,PM}L$ product still holds. However, to measure the voltage required to induce a π-shift ($U_{\pi,PM}$) is slightly more complicated. One way to measure $U_{\pi,PM}$ of a phase modulator is to place it in one arm of an external Mach-Zehnder interferometer. In this configuration U_π can be measured as described above for the case of an MZM. An alternative approach to measure U_π without the need of an external MZI is to measure the modulation index of the phase modulator [35, 82], Fig. 11(d).

The phase modulator shifts the phase of an optical signal or optical carrier proportional to the applied voltage. The applied and the length of the modulator defines the phase-shift induced on the optical carrier. If the applied driving field is time-variant, the phase modulation can be translated to a frequency modulation, which generates modulation sidebands in the optical response of the PPM. These modulation sidebands can be measured by an optical spectrum analyzer (OSA). The transfer function of the PPM is given by

$$\frac{E_{out}(t)}{E_{in}} \propto A \cdot \exp(j\gamma(t)), \tag{19}$$

where $\gamma(t)$ is the electrical driving signal and A is the amplitude response of the modulator. The incoming optical carrier can be described by a time-variant expression $E_{in} = A_0 \cdot \exp(j\omega_0 t)$, where A_0 is the initial amplitude; ω_0 is the carrier angular frequency. When a sinusoidal, low-frequency phase modulation $\gamma(t) = \eta\sin(\Omega t)$ with an amplitude η and a frequency $\Omega \gg \omega_0$ is applied to the carrier, the modulated output signal can be described by $E_{out}(t) = A \cdot A_0 \cdot \exp\left(j\left(\omega_0 t + \eta\sin(\Omega t)\right)\right)$. The expression can be expanded by the Jacobi-Anger identity and simplified by the relation $J_n(-\eta) = (-1)^n J_n(\eta)$,

$$E_{\text{out}}(t) = A_{\text{out}} \exp\left(j\left(\omega_0 t + \eta \sin(\Omega t)\right)\right) = A_{\text{out}} \exp\left(j\omega_0 t\right) \exp\left(j\eta \sin(\Omega t)\right)$$

$$= A_{\text{out}} \exp\left(j\omega_0 t\right)\left(\sum_{n=-\infty}^{\infty} J_n(\eta) \exp\left(jn\Omega t\right) \right) \tag{20}$$

$$= A_{\text{out}} \exp\left(j\omega_0 t\right)\left(J_0(\beta) + \sum_{n=1}^{\infty} J_n(\eta) \exp\left(jn\Omega t\right) + \sum_{n=1}^{\infty} (-1)^n J_n(\eta) \exp\left(-jn\Omega t\right) \right),$$

where $J_n(\beta)$ are Bessel functions of the first kind. The measurable optical spectrum of the signal is given by

$$E_{\text{out}}(\omega) = A_{\text{out}}\left(J_0(\eta)\delta\left(\omega - \omega_0\right) + \sum_{n=1}^{\infty} J_n(\eta)\delta\left(\omega - (\omega_0 + n\Omega)\right) + \sum_{n=1}^{\infty} (-1)^n J_n(\eta)\delta\left(\omega - (\omega_0 - n\Omega)\right) \right)$$

$$(21)$$

The modulation of the optical carrier results in an energy transfer from the optical carrier (J_0) to the nth-order sidebands (J_n). For small signal modulation ($\eta \lesssim 1.84$) the modulation index η can be derived from the sideband-to-carrier power ratio ΔP by evaluating the ratio of the zero and first order Bessel functions of the first kind,

$$\Delta P = \frac{P(\omega_0 \pm \Omega)}{P(\omega_0)} = \frac{J_1(\eta)^2}{J_0(\eta)^2} \tag{22}$$

The ratio between the first-order modulation sidebands ($n = 1$) and the optical carrier is maximum when the optical carrier is suppressed completely ($J_0(\eta \approx 2.4) = 0$). The most energy is found in the first-order modulation sidebands at $\max(J_1(\eta))$ at $\eta \approx 1.84$. For large-signal modulation one may investigate the power ratio of the carrier to higher-order sidebands, depending on the amplitude of the corresponding Bessel function of the first kind.

This way modulation depth can be measured using an optical spectrum analyzer (OSA) to determine the power level of the optical carrier and the modulation sideband. The experimental setup is depicted in Fig. 11(d). Knowing the modulation index, one can calculate $U_{\pi,\text{PM}}L$ of a phase modulator using,

$$\frac{U_{\pi,\text{PM}}}{U_d} = \frac{\pi}{\eta}$$

$$U_{\pi,\text{PM}}L = \frac{U_d}{\eta} \cdot \pi \cdot L, \tag{23}$$

where U_d is the applied driving voltage and L is the device length.